Solar Energy Materials & Solar Cells 237 (2022) 111557

Contents lists available at ScienceDirect

Solar Energy Materials and Solar Cells

journal homepage: www.elsevier.com/locate/solmat

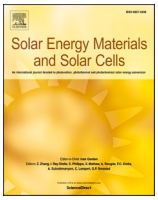

Past research and future strategies for molten chlorides application in concentrated solar power technology

Mickael Lambrecht *, María Teresa de Miguel, María Isabel Lasanta, Francisco Javier Pérez

Surface Engineering and Nanostructured Materials Research Group, Complutense University of Madrid, Complutense Avenue s/n, Madrid, Spain

A B S T R A C T

This review summarizes past research and future strategies for the improvement of the pair heat transfer fluids (HTF) - containing material, used in concentrated solar power (CSP) plants, focusing on the most interesting and promising HTF, chloride molten salts. Indeed, their low cost and operating range temperature make them very strong potential candidates for future CSP plants, furthermore improvable by wisely adding nanoparticles. Nevertheless, their well-known aggressive behaviour entails selecting a long-lasting resistant alloy, which requires a better understanding of its associated corrosion mechanisms and the influences of its alloying elements. Mitigation strategy mechanisms that come from salt impurities implying purification processes are also reviewed. Finally, thermogravimetric analysis (TGA) coupled with differential scanning calorimetry (DSC) for salt preparation, and numerical simulations on Thermocalc software modelling elements activities of selected alloys and their interaction with molten chlorides are discussed.

1. Introduction

The strong desire to produce electricity with the lowest impact on the environment tends to design and improve new renewable energy systems. Concentrated solar power (CSP) plants with thermal energy storage (TES) are emerging as one kind among the most promising ones. Indeed, HTF and TES means such as molten salts are the determining factor for achieving a viable electricity generation, aiming at the Sunshot goal dealing with the reduction of the molten salts cost to under 15 USD/kWh in CSP plants (energy.gov/eere/solar/sunshot-2030). Enhancing the performance compels work at a wider operating temperature range, inducing the design of new salts. Moreover, temperatures of 700–800 °C are being projected to fully utilize Advanced Supercritical Carbon Dioxide (S–CO_2) Brayton Cycles [1,2]. The selection of the future salts will be made on their operating ranges, specific heat capacities and costs. Indeed, a better performance is targeted by a mixture of single salts. Fig. 1 gathers different families of salts reported in literature, along with their temperature ranges and costs. Based on these two criteria, the most attractive are chloride salts, MgNaK ternary chloride offering a lower cost and ZnNaK chloride a wider temperature range [3–5].

Indeed, studies on chloride salts for CSP plants have emerged in the past 15 year as we can see on Fig. 2, representing the number of articles dealing with this subject with the keywords “chloride salts; solar; CSP” from 2004.

The properties of the molten chloride salts will be determined by their composition and proportion of each component. Single chloride salts properties are overviewed in Table 1:

Firstly, regarding the necessary low melting temperature (T melting) and high temperature stability of the salt (T degradation) in a CSP plant, some single chloride salts should be avoided. Indeed, $AlCl_3$ and $FeCl_3$ have a strong vapour pressure that limit their use, reaching 1 bar at 180 °C and 330 °C, respectively, thus demanding an unacceptable pressurization cost. The use of $ZnCl_2$ can lower the melting point temperature, but its vapour pressure reaches 1 bar at 720 °C, which is still acceptable for the operating temperatures. For example, the ternary ZnNaK chloride presents a stability of up to 850-900 °C.

On the other hand, the heat capacity (Cp) must be optimized with the cost of the molten chloride salt. Table 2 presents a comparison of single salt costs from different sources: Sigma Aldrich for lab scale (per kilogram) with their quality, and from companies selling in bulk (per ton converted to per kilogram) which are referenced. Obviously, for CSP plants, the bulk prices are chosen, whereas laboratory experiments are conducted with high quality products. The most performant one is the lithium chloride (LiCl) salt. Nevertheless, it is also the most expensive (indeed, RbCl or CsCl are irrelevant to this application due to their costs). But the second one is the sodium chloride (NaCl) which is the cheapest, with a Cp of 1.1 kJ/(kg.K) and for 0.05 USD/kg. Most of the chloride salt mixtures contain KCl and/or NaCl because of their relatively good Cp and cost. Then $MgCl_2$ based chloride compared to $ZnCl_2$-based salt, will have a lower Cp but a greater operating temperature. The cost per euro has been converted per US dollar with the price market

* Corresponding author.
E-mail address: milambre@ucm.es (M. Lambrecht).

https://doi.org/10.1016/j.solmat.2021.111557
Received 25 August 2021; Received in revised form 15 December 2021; Accepted 18 December 2021
Available online 27 December 2021
0927-0248/© 2022 The Authors. Published by Elsevier B.V. This is an open access article under the CC BY-NC-ND license (http://creativecommons.org/licenses/by-nc-nd/4.0/).

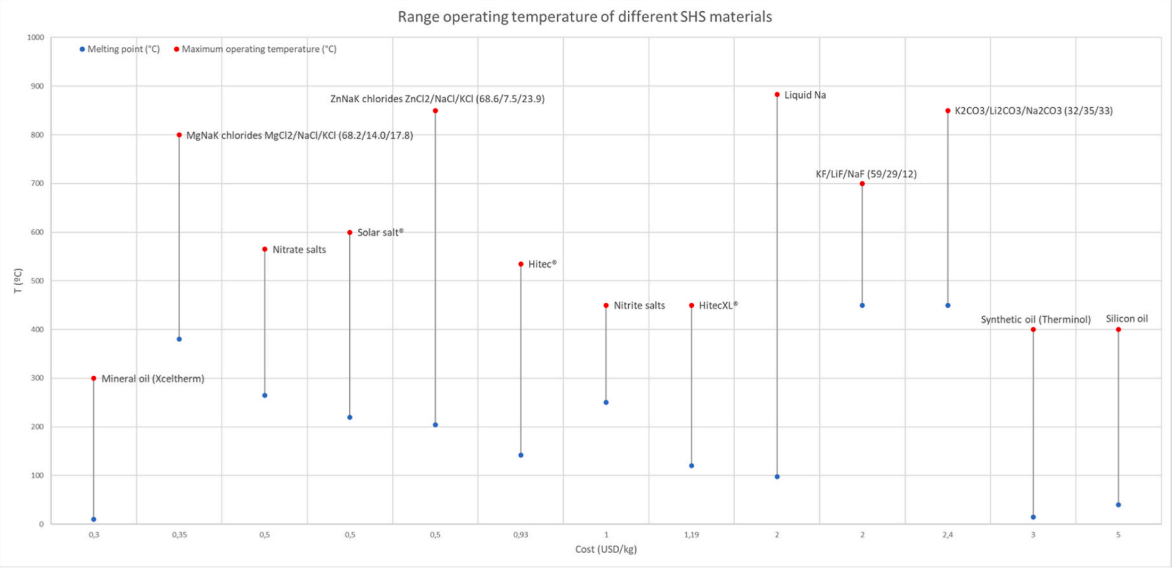

Fig. 1. Range operating temperature of different materials for sensible heat storage (SHS) with their respective costs.

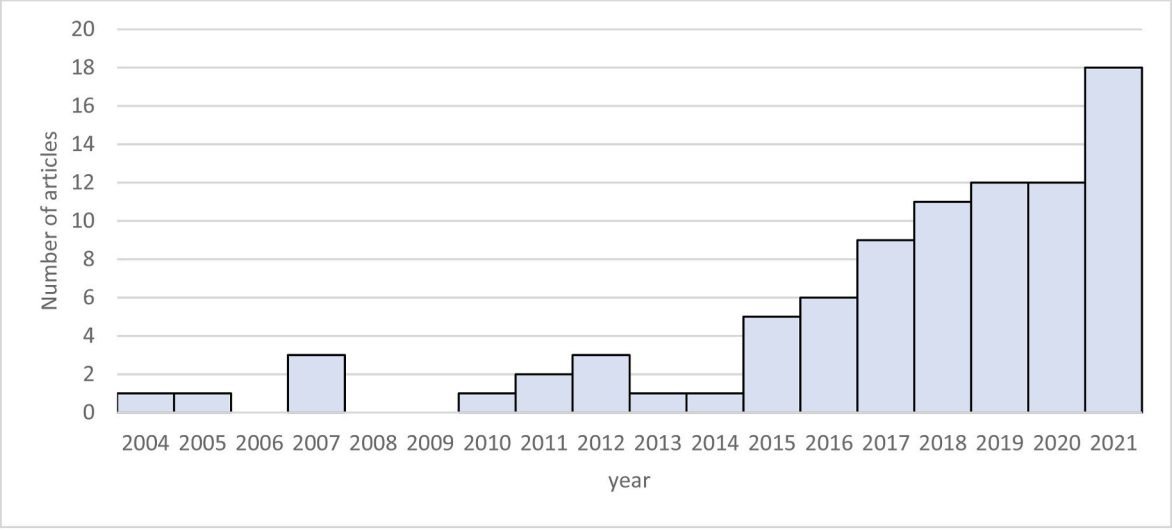

Fig. 2. Number of publications per year since 2004 with the keywords "chloride salts; solar; CSP" from: science direct.

Table 1
Thermo-physical properties of single chlorides.

Single chlorides	T melting [6,7] (°C)	T degradation [6](°C)	Hydrates phases [6]	Heat capacity (liquid) (kJ kg-1 K-1) [8,9]	Temperature when the vapour pressure reaches 1 bar (°C) [9]
AlCl3	193	180	6	0,94	180
BaCl2	961	1560	2	0,52	N/A
CaCl2	775	1935	1,2,4,6	0,92	>2150
FeCl3	308	316	6	0,83	330
(FeCl2)	677	1023	2,4	0,81	N/A
KCl	771	1420	0	0,99	1400
LiCl	610	1383	1	1,5	1380
MgCl2	714	1412	1,2,4,6	0,97	1390
NaCl	801	1465	0	1,1	1430
SrCl2	876	1250	6	0,66	N/A
ZnCl2	290	732	1/1,5/ 2,5/3/4	0,74	720
MnCl2	650	1190	2,4		

ratio of July 2021: 1€ = 1.19$

To operate in a CSP plant, the salt must keep its thermal properties unchanged over time.Q. Yan, Q. Fan [10] studied the repeatability of the properties of binary KLi and ternary KLiNa chloride salts, represented on Fig. 3, and gave the same conclusion for both, as they carried a good cyclic stability despite a ten times larger variation of the phase latent heat temperature than the phase transition temperature (2–6% and 0.2 to 0.6%respectively). This means that the operating range temperature remains the same whereas the performance is more damaged.

Fig. 4 presents examples of the cost per kWh (cost of the quantity of energy delivered per hour) of some salts mixtures with their respective operating range and specific heat capacity. Indeed, Li-, Rb-, Sr- or Cs-based salts are inappropriate for this application due to their high cost. Thus, $ZnCl_2$ -based salts are the most expensive of the choosable ones but their great operating range (204 °C to more than 800 °C) makes them attractive. On the other hand, quaternary Na–K–Mg–Ca chloride has proven to have excellent properties with a Cp of 1.42 kJ/(kg.K) in a range of between 385 °C to more than 800 °C, and low cost (3.89 USD/kWh). Ternary and quaternary chloride salts seem to be the most

Table 2
Costs of single chloride salts from literature, Sigma Aldrich, and Company.

Reference	Sigma Aldrich (Lab)		Alibaba (per ton– > per kg)		
Salt	Cost $/kg	Quality	Cost $/kg	Quality	Company
$CaCl_2$	100	anhydrous, granular, ≤7.0 mm, ≥93.0%	0.145	94%	Weifang Senrui Chemical Co., Ltd.
KCl	163	ACS reagent, 99.0–100.5%	0.34	99% Industrial grade	P.M. THANGIAH NADAR
LiCl	488	ACS reagent, ≥99%	7.8	High quality 99% CAS 7447-41-8 anhydrous	Inner Mongolia Pulisi Chemical Co., Ltd.
$MgCl_2$	92,5	powder, <200 μm	0.22	99% purity	Weifang Xiangyun Chemical Co.
NaCl	44,3	ACS reagent, ≥99.0%	0.05	99%industry grade	Shouguang Dinghao Trading Co.
$SrCl_2$	15613	anhydrous, powder,≥99.99% trace metals basis	100	99%–99.5% anhydrous	Shanghai Ruizheng Chemical Technology Co., Ltd.
$ZnCl_2$	149	anhydrous, free-flowing, Redi-Dri™, reagent grade, ≥98%	1	0.96%	Taian Health Chemical Co., Ltd.
$MnCl_2$	124,5	beads, 98%	1.5	N/A	Shanghai Ruizheng Chemical Technology Co., Ltd.
RbCl	4450	ReagentPlus®, ≥99.0% (metals basis)	500	99%–99.9%	Anhui Jin'ao Chemical Co., Ltd.
CsCl	3296	ReagentPlus®, 99.9%	105.8	99.9%	Jiangxi Royal Import & Export Co., Ltd.
Addition of Nanoparticles					
Al_2O_3	4627	nanopowder, <50 nm particle size (TEM)	20	N/A	Shanghai Xinglu Chemical Technology Co., Ltd.
Expanded Graphite (EG)	N/A	N/A	0.96	Nature flake graphite 895	, Qingdao Furuite Graphite Co., Ltd.

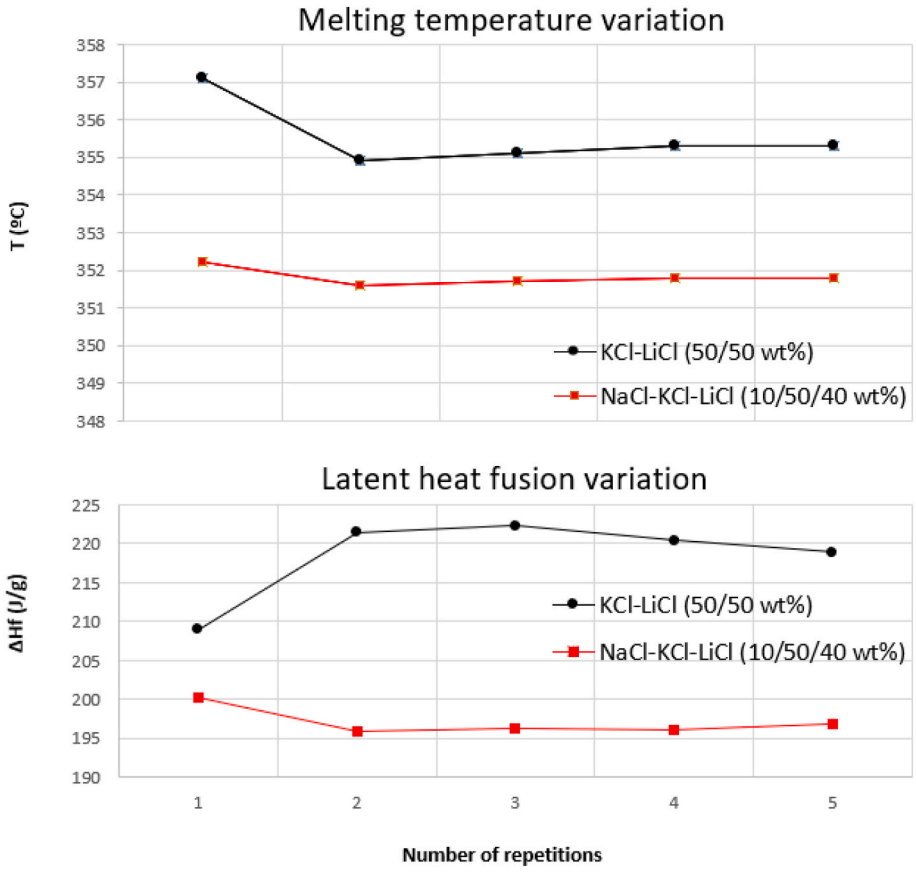

Fig. 3. Thermal cycling variation of melting temperature and latent heat fusion of binary KCl–LiCl and NaCl–KCl–NiCl.

promising salts, but can be improved in terms of operating range temperature and Cp considering single salts addition, such as $ZnCl_2$. It would make it possible to achieve competitive costs under the 15USD/kWh goal and increase the operating range. Regarding the main elements suitable for promising molten chloride, ternary eutectics of Na, K, Zn, Mg and Ca with melting temperatures and costs are presented in Table 3. Eutectic temperatures were graphically obtained from ternary phase diagrams [Factsage database] [11]. The most interesting chloride salts relying on their melting points and costs are ZnKCa (1,44/35,37/63,19 wt%) with [$T_{eutectic}$ = 229.37 °C; 0.23$/kg], ZnNaK (68.67/7.22/24.10 wt%) with [$T_{eutectic}$ = 227 °C; 0.77$/kg] and MgNaK (53.41/20.97/25.62 wt%) with [$T_{eutectic}$ = 382.01 °C; 0.22$/kg]. DSC experiments are necessary to measure their specific heat and thus evaluate their performance. These costs take into account the hydrated components of the salts, and are thus ponderated with the real amount needed of single salts to obtain the exact eutectic after dehydration. This point will be detailed and discussed later in this paper.

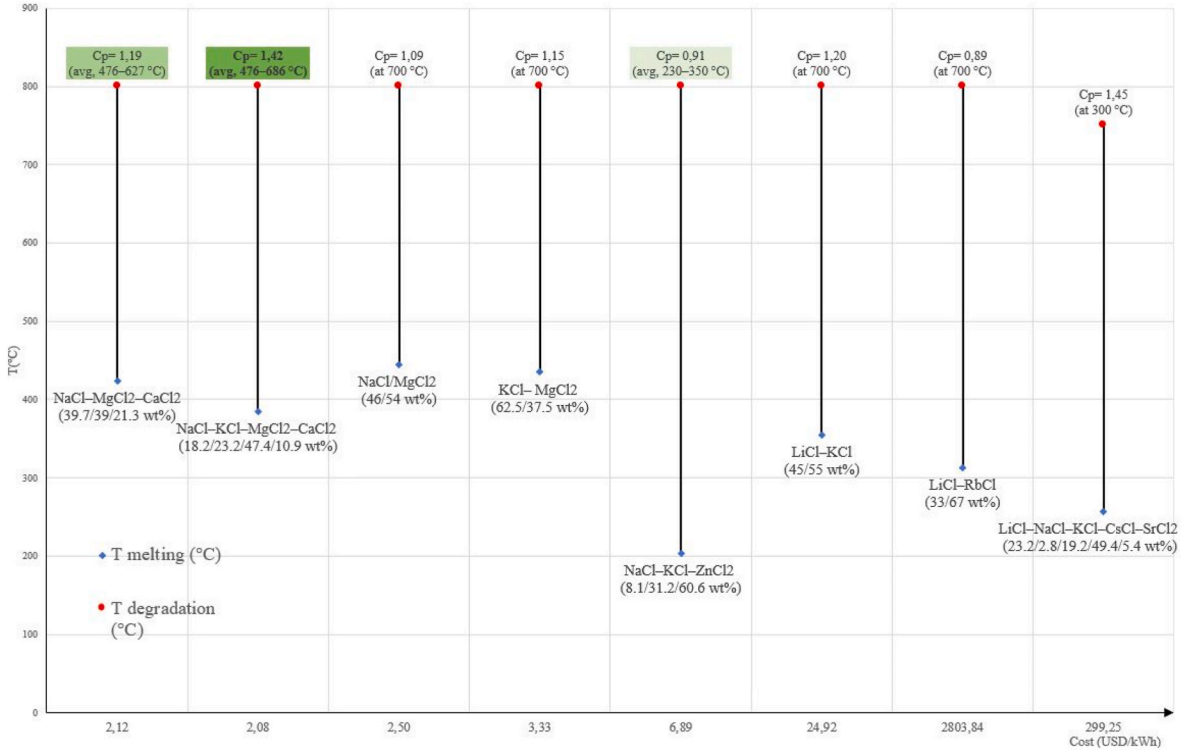

Fig. 4. Cp of some salts with their operating range temperature and their respective cost per kWh.

Table 3
Potential eutectic chloride salts with their cost per kilogram from Sigma Aldrich and companies.

Chloride Salt	% mass	Eutectic Temperature(°C) [reference]	Cost($/kg) (Sigma aldrich(LAB))	Cost($/kg) (Alibaba per ton– > per kg)
(MgNaK)Cl	53.41/20.97/25.62	382.01 [Factsage]	161.49	0.35
(MnKNa)Cl	44.15/47.25/8.60	382.45 [Factsage]	140.36	0.83
	64.47/38.19/21.21	381.62 [Factsage]	157.01	1.11
(ZnKCa)Cl	1.44/35.37/63.19	229.37 [Factsage]	191.60	0.32
(MgZnNa)Cl	0.86/82.29/16.85	252 [11]	203.03	1.27
(MgZnK)Cl	1.77/67.08/31.16	228 [11]	213.89	1.14
(CaZnNa)Cl	1/82.17/16.83	252 [11]	202.03	1.27
(ZnNaK)Cl	68.67/7.22/24.10	227 [11]	205.47	1.14
(ZnMgCa)Cl	97.77/1.41/0.82	312 [11]	234.53	1.50
Compared with commercial salts			**Cost ($/kg)**	
Solar salt (KNO_3–$NaNO_3$)	60/40	220 [12]	0.50	
HITEC ($NaNO_3$–KNO_3–$NaNO_2$)	7/53/40	142 [12]	1.1	
HITEC XL ($NaNO_3$–KNO_3– $Ca(NO_3)_2$)	7/45/48	130 [12]	0.9–1.19	

2. Enhancement of properties

Otherwise, the properties of the molten salts can be enhanced by the addition of nanoparticles to obtain a so-called “molten salt-based nanofluid” (MSBNF). Researches has been conducted on the addition of different nanoparticles on molten salts and their effect on their specific heat, thermal conductivity and viscocity. Most of the published research gather nanoparticles additions over nitrate, nitrite and carbonate mixtures. Only few investigations have been performed over chlorides formulations so far.

2.1. Specific heat (Cp)

The specific heat of a HTF determine its performance, as it is an intensive property which represents the capacity of the fluid to accumulate heat per degree and per mass. Fig. 5 presents the data of enhancement of Cp with nanoparticles obtained from literature. For the enhancement of Cp, the vaddition of SiO_2 and Al_2O_3 has demonstrated the best improvement, with 14.50% for BaNaCaLi chloride at 1 wt% SiO_2 [13] and 13.70% for MgNaK chloride at 0.7 wt% Al_2O_3 [14]. Then 1 wt% of Mg nanoparticles in the binary NaCa chloride (with 52-48 M ratio) increased the specific heat capacity by 10% [15].

2.2. Thermal conductivity

Thermal conductivity remains a key factor to better optimize heat transfer properties. Fig. 6 presents the different studies on this property improvement on nanofluids. The best enhancement has been demonstrated by MultiWall Carbon NanoTubes (MWCNT) with 293% for the solar salt [16] and then expanded graphite (EG) with 177.51% for the ternary MgNaCa chloride salt [17], reaching 2.084W/(m.K), competing with LiNaK carbonate with its 2.191 W/(m.K) enhanced by Al_2O_3 nanoparticles [18]. Indeed, the disadvantages that chloride salts could represent compared to others can be balanced by the addition of nanoparticles. Nevertheless, those nanoparticles must be controlled in term of concentration, size, and fabrication process. The variation of the

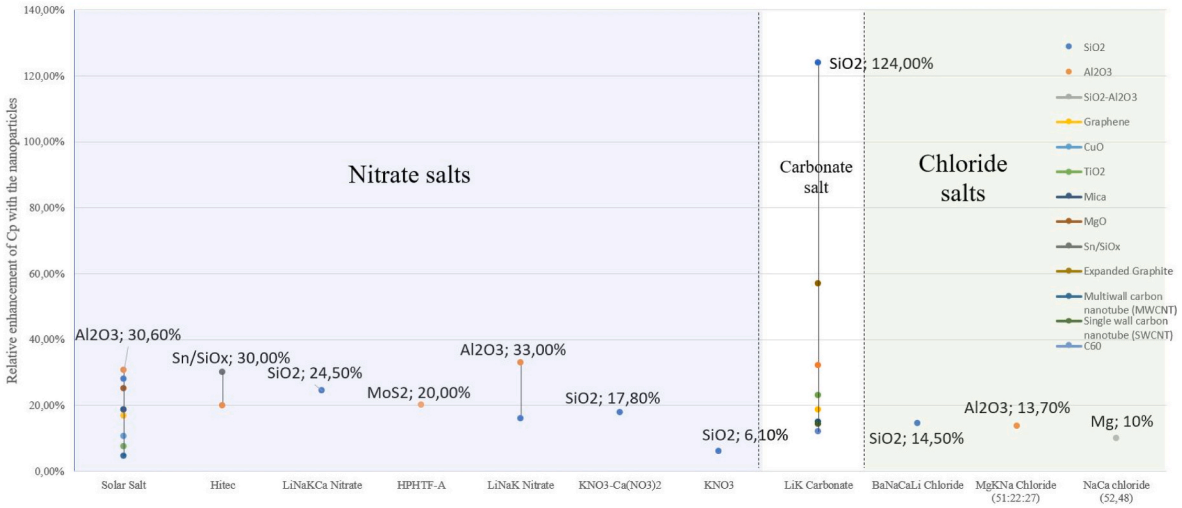

Fig. 5. Enhancement of the specific heat of molten salts with their respective nanoparticles addition.

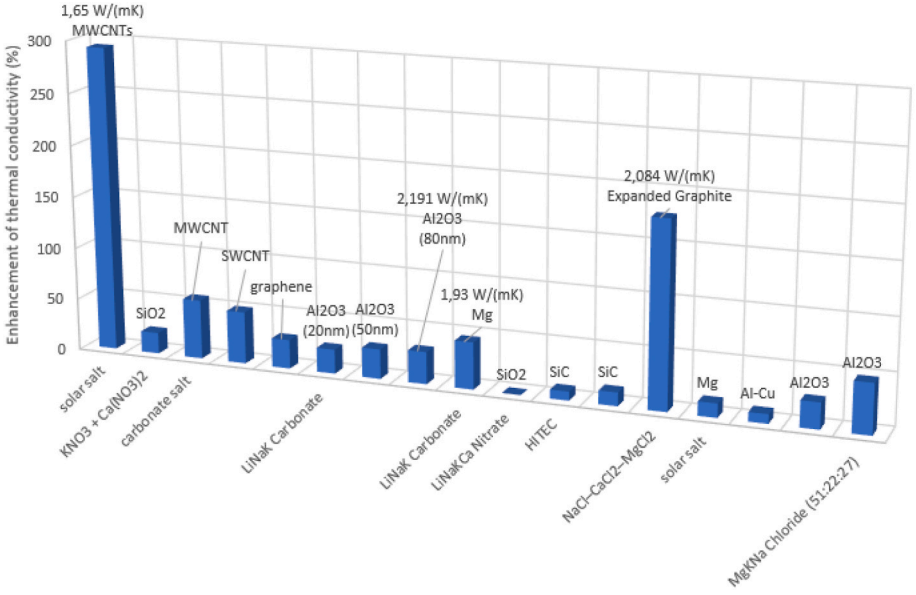

Fig. 6. Enhancement of thermal conductivity of molten salts mixture with nanoparticles.

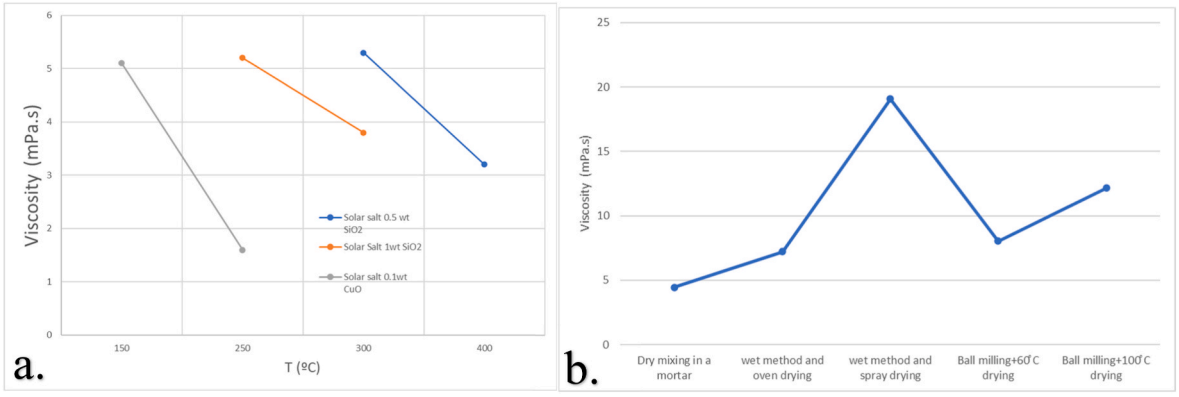

Fig. 7. –Viscosity dependence of a. temperature and nano-addition. b. fabrication process (for Solar Salt).

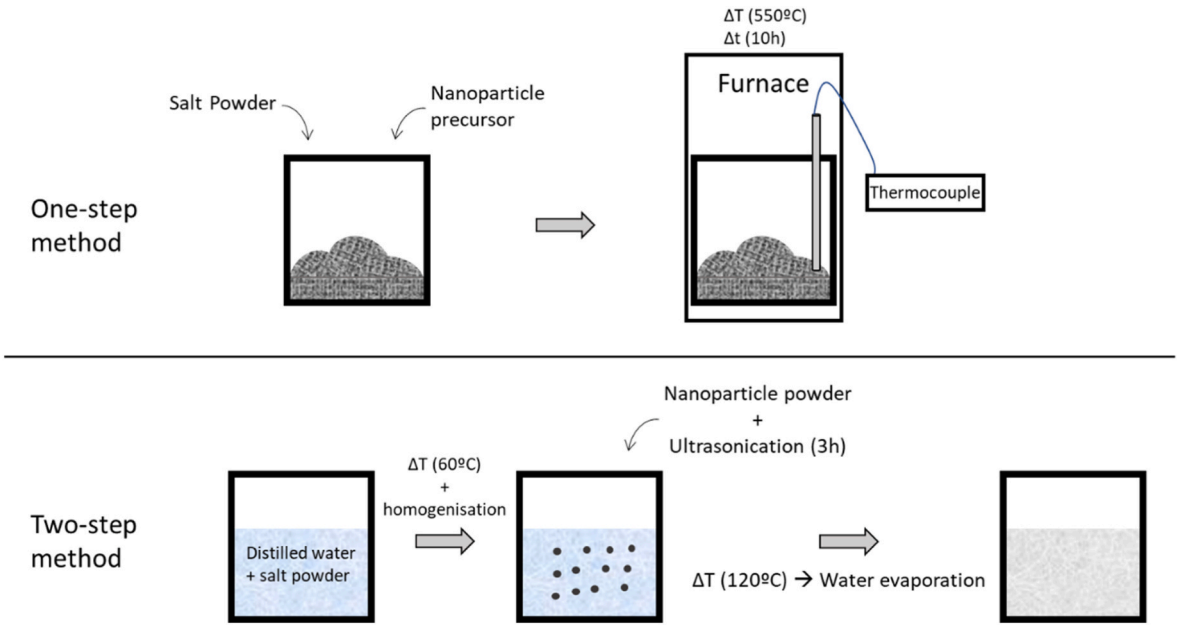

Fig. 8. representation of one-step and two step methods of the preparation of nanofluids.

enhancement of the thermal conductivity by the size of the nano particles is also remarkable. For the LiNaK carbonate, 1 wt% of Al_2O_3 nanoparticles with 20 nm and 50 nm size, showed an increase of 23.3% and 28.5% respectively. With an 80 nm size at 0.8 wt%, it rises to 30.9%. For the HITEC salt, a variation from 0.6 wt% to 0.72 wt% of SiC gives a variation of the enhancement of 4.4% [19,20].

2.3. Viscosity

The variation of the viscosity, with temperature, must be considered when adding nanoparticles. Fig. 7.a. presents the viscosity dependence of temperature and its nano-addition for the Solar Salt Indeed, although the Cp has been enhanced by 10.48% with CuO and 28% with SiO_2, a stronger diminution of viscosity is shown with CuO nanoparticles (5.1–1.6 mPa s from 150 °C to 250 °C) than with SiO_2 ones. It can be remarked that the concentration could also be optimized as the 1 wt% SiO_2 addition has a better behaviour than the 0.5 wt% SiO_2 at 300 °C, with 3.8 and 5.2 mPa s, respectively [21,22].

The fabrication process of the nanoparticles also has an impact on viscosity, as seen on Fig. 7.b [23]. For the Solar Salt, a dry mixing in a mortar shows the best performance, followed by the wet method with oven drying.

The two processes are schematized on Fig. 8. Even though the first one is more expensive because of the cost of the precursors, other costs will be related to the purification of the second one. Indeed, ternary MgNaK and ZnNaK chlorides do not have an inert behaviour in water. The major challenge is to avoid a chemical reaction between the salt and the distilled water to form corrosive (Mg,Zn)OHCl.

It remains to be seen if enhancing the viscosity properties with this method does not negatively impact on the other properties, as happened when the choice of the nanoparticles for the enhancement of the Cp was not the best for the viscosity.

3. Salt preparation and corrosion mitigation

3.1. Purification of salts

Magnesium chloride-based salts are among the best HTF candidates and have already been studied for this application [3,24–35]. Nevertheless, their well-known hygroscopic property requires a purification due to the hydrate phases absorbed, mainly during the manipulations of the salt, which diverts its eutectic composition and thus makes the experiments inaccurate. Research has been conducted on the salt preparation to optimize its purity by lowering hydrate concentration and thus the corrosive species. Smith and Veazey [36] used the vapour pressure curves of $MgCl_2{\cdot}n(H_2O)$, clarified in Fig. 10, to determine the different temperature steps in the process of purification. A cascade sequence of four stages describes the dehydration but also the decomposition reactions as follows:

Stage I: $MgCl_2{\cdot}6H_2O \rightarrow MgCl_2{\cdot}4H_2O + 2H_2O$ (1)

Stage II: (a) $MgCl_2{\cdot}4H_2O \rightarrow MgCl_2{\cdot}2H_2O + 2H_2O$ (a): Dehydration (2)

(b) $MgCl_2{\cdot}4H_2O \rightarrow MgOHCl + HCl + 3H_2O$ (b): Decomposition (3)

Stage III: (a) $MgCl_2{\cdot}2H_2O \rightarrow MgCl_2{\cdot}H_2O + H_2O$ (4)

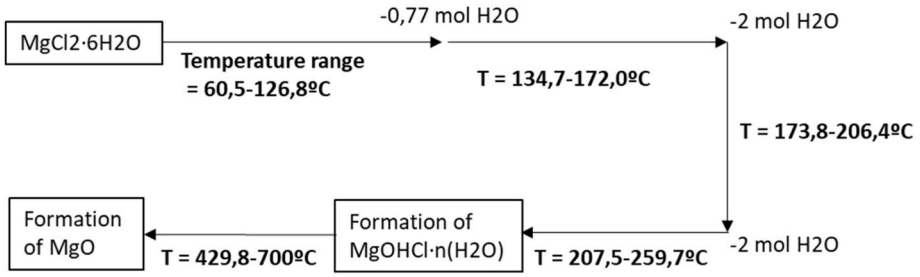

Fig. 9. Dehydration process of $MgCl_2{\cdot}6H_2O$ by Zhang and al. Lu [37].

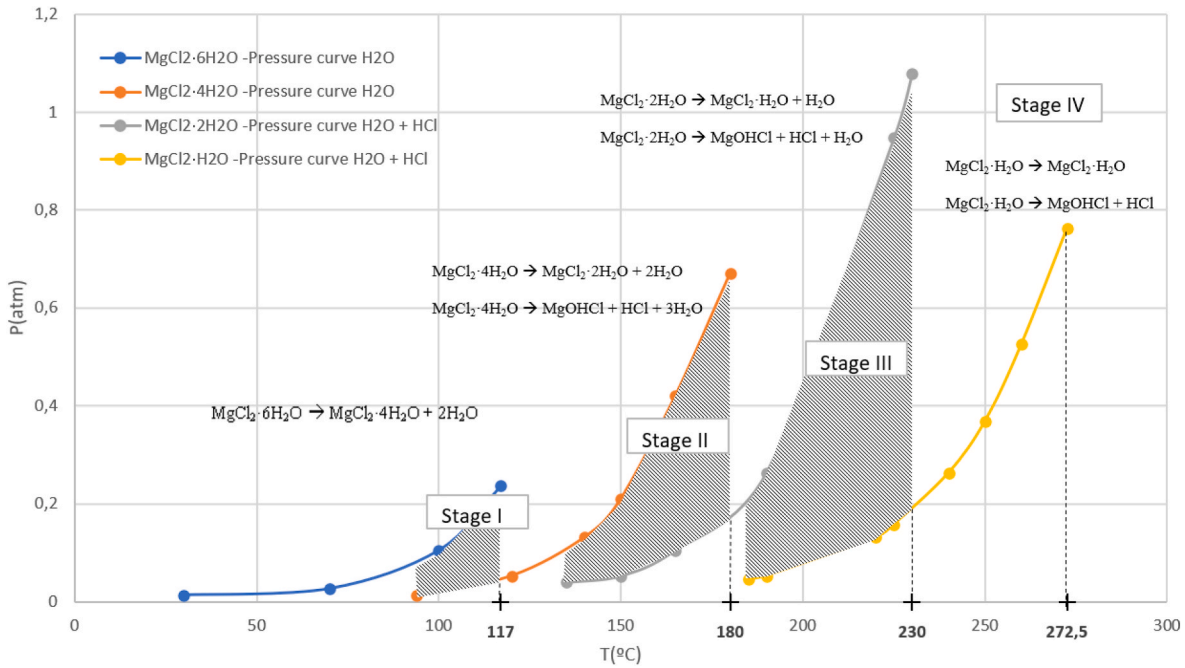

Fig. 10. Dehydration process of $MgCl_2{\cdot}nH_2O$ by Veazey and al [36].

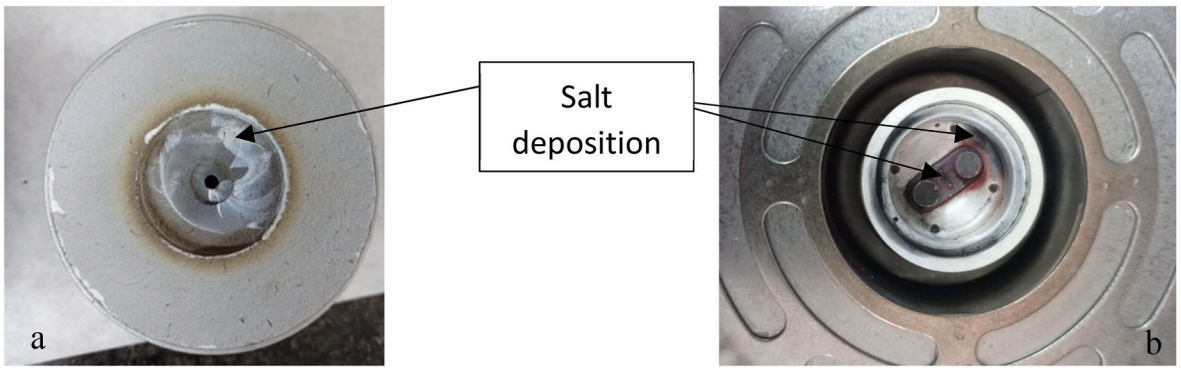

Fig. 11. Salt deposition on a. cell protector and b. cell sensor.

(b) $MgCl_2{\cdot}2H_2O \rightarrow MgOHCl + HCl + H_2O$ (5)

Stage IV: (a) $MgCl_2{\cdot}H_2O \rightarrow MgCl_2 + H_2O$ (6)

(b) $MgCl_2{\cdot}H_2O \rightarrow MgOHCl + HCl$ (7)

Indeed, the optimal temperatures are 117 °C, 180 °C, 230°c and 272.5 °C for each stage, respectively (Z. Zhang, X. Lu [37]). proposed an equivalent process schematized in Fig. 9, but with five temperature ranges to obtain the dehydrated $MgCl_2$.

Nevertheless, Epstein et al. [38] and Long et al. [39] showed that when anhydrous $MgCl_2$ reaches temperatures above 450 °C, Cl_2, HCl and MgO are present, identifiable as the products of the reaction (8). Therefore, the anhydrous $MgCl_2$ obtained by dehydrating $MgCl_2{\cdot}6H_2O$ could easily hydrolyse at elevated temperature.

$$4MgCl_2(s)+O_2(g)+2H_2O(g) = 4MgO(s)+4HCl(g)+2Cl_2(g) \quad (8)$$

This cheap method is not effective for impurity removal at low concentration because of its thermodynamic instability, with a dangerous production of gases like HCl.

J.C. Vidal and N. Klammer [26] proposed a method considering the decomposition of MgOHCl into MgO and HCl at 554 °C, and thus added steps of 2 h at 400° and 30 min at 600 °C followed by cooling to 117 °C.

3.1.1. *Differential scanning calorimetry (DSC) measures*

To confirm the different steps of salt dehydration, DSC experiments were performed on $MgCl_2{\cdot}6H_2O$, $ZnCl_2{\cdot}4H_2O$, (MgNaK)Cl (53.41/20.97/25.62 wt%) hydrated salt with a Q20 TA instrument equipment (50 ml/min Nitrogen flow, 10 °C/min, Alumina crucible) from 40 °C to 500 °C with two cycles of heating and cooling to remark the sample's dehydration. The crucibles were encapsulated and perforated with a 0.60 ± 0.05 μm hole in order to let the steam generated escape and determine the influence of vapour pressure on the transformations. The mass loss was coupled with heat flow, with a Q600 TA instrument equipment (100 ml/min Nitrogen flow, 10 °C/min, Sapphire open crucible). Indeed, the heat flow signal of Q20 is much more precise and will thus be used for the identification of the different processes.

Regarding the molar mass of $MgCl_2$, $MgCl_2{\cdot}6H_2O$ and $ZnCl_2$, $ZnCl_2{\cdot}4H_2O$, the mass loss of dehydration can be theoretically estimated with a mass ratio of 2.13 and 1.53, respectively. As seen on Fig. 11, white aspect salt deposition occurred on the thermoelectric disk and the thermocouple, so not only dehydration occurred, and the salt's composition deviates from its eutectic. Indeed, it comes from the decomposition of the salt.

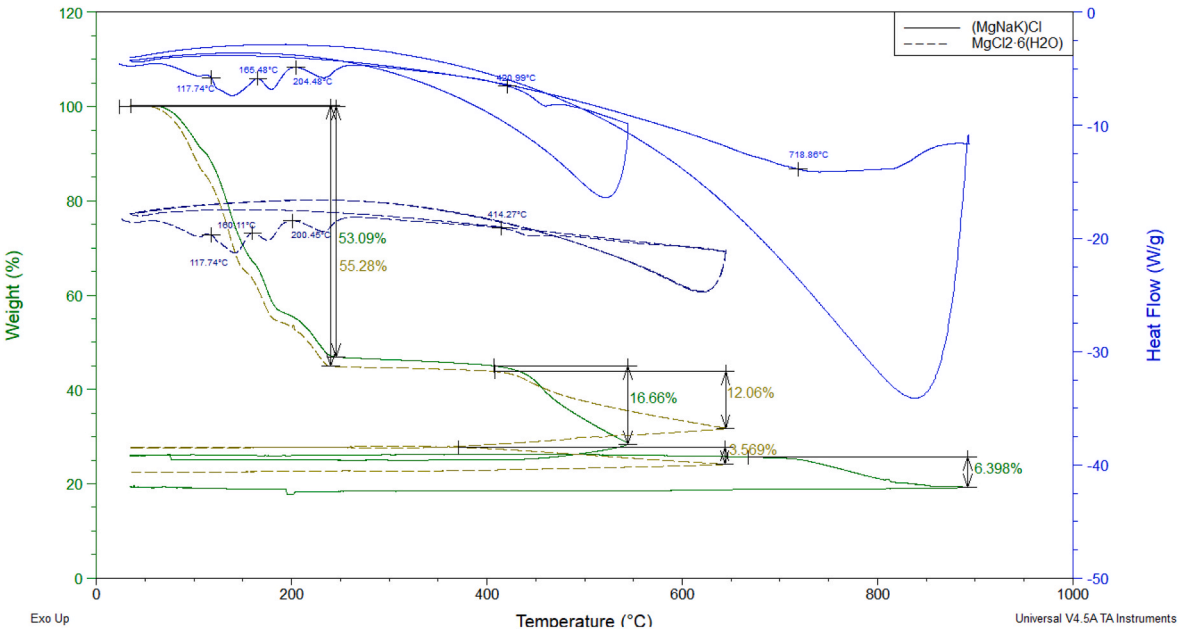

Fig. 12. Q600-DSC/TGA measures of (MgNaK)Cl and $MgCl_2{\cdot}6H_2O$.

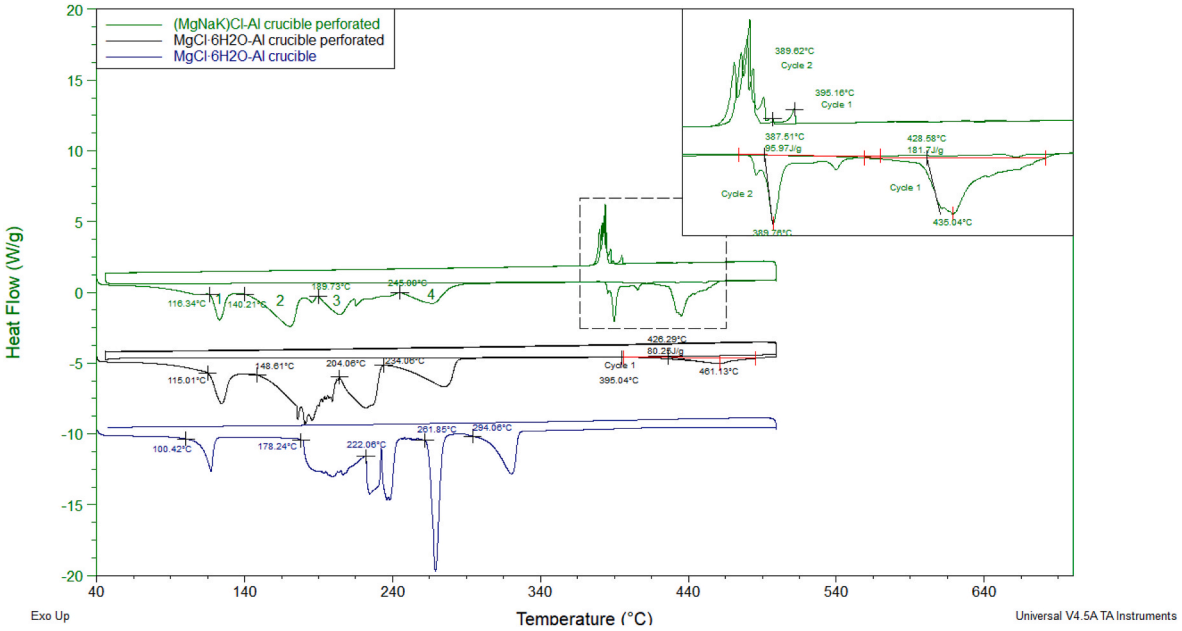

Fig. 13. Q20-DSC measures of (MgNaK)Cl, open and closed $MgCl_2{\cdot}6H_2O$.

Fig. 12 and Fig. 13 show DSC/TGA measures with Q600, and Q20 respectively on MgCl2·6H2O and hydrated (MgNaK)Cl (53.41/20.97/25.62 wt%). The dehydration process is observable as multiple steps in both equipments, but with discrepancies on the temperature that are certainly due to their precision. During the first cycle of heating, Q600 shows endothermic peaks at 60 °C, 117 °C, 160 °C and 200 °C for $MgCl_2$ and 60 °C, 117 °C, 165 °C and 204 °C for (MgNaK)Cl, with a partial mass loss of 55% and 53%, respectively. Then a second mass loss of 12–16% occurs at 414-420 °C with an endothermic peak that may be identified as the conversion of MgOHCl into solid MgO and gaseous HCl and Cl_2. When cooling to the initial temperature, no peak is measured for any salt, as can be seen in Fig. 12. Indeed, when reheating, the weight and heat flow remain constant for the same temperature range reflecting successful dehydration. Plus, a mass loss of 6.4% is still measured with endothermic peaks at 718 °C to 850 °C that could stem from the degradation of the salt. This excess of mass loss may be due to the Nitrogen flow that helps the vaporization of the salt. Melting and crystallization temperatures are not detected and thus the use of a better signal is necessary.

On Fig. 13, Q20 DSC measures shows a better signal with four well-defined dehydration endothermic peaks at 116.34 °C, 140.21 °C, 189.73 °C and 245.00 °C for (MgNaK)Cl. Indeed, $MgCl_2{\cdot}6H_2O$ showed a different behaviour when trapped in the crucible, from when with a perforated lid, due to the pressure and condensation of the gas, delaying the process at a higher temperature for each step. Moreover, as seen with Q600 measurements, an endothermic peak is detected at 400 °C for MgNaK(Cl) and 395 °C for open-$MgCl_2$ with 191.5 J/g, and 80.25 J/g respectively. No peaks are recorded for closed-$MgCl_2$ at that

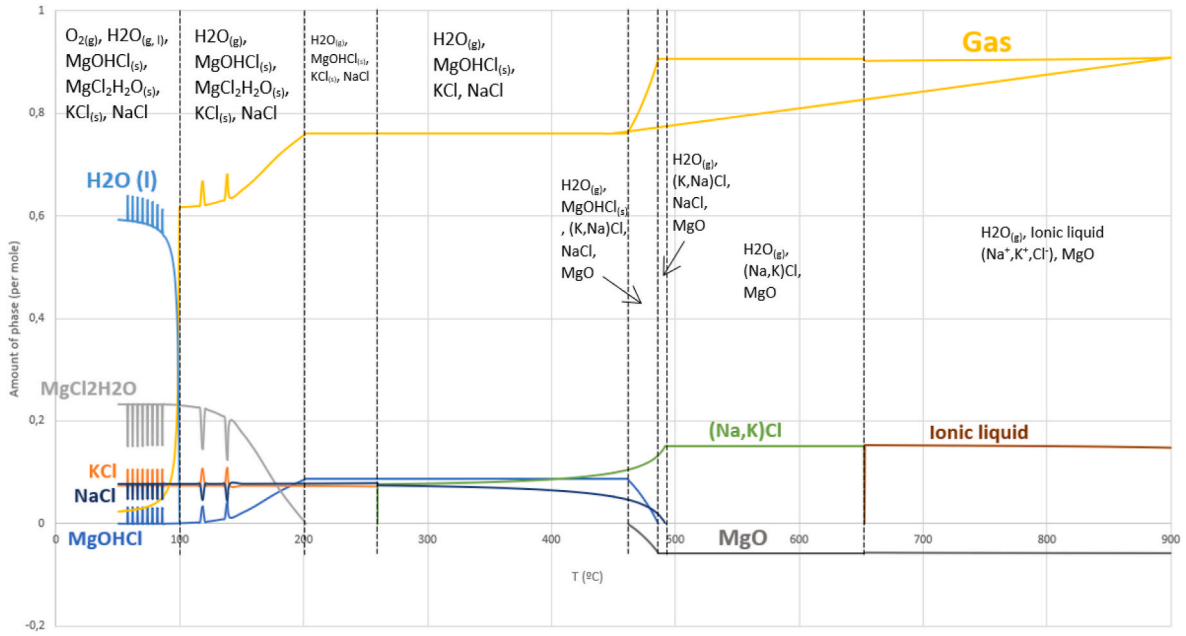

Fig. 14. Thermocalc simulation of the behaviour of hydrated (MgNaK)Cl salt with temperature.

temperature. An MgO precipitation can be identified as this peak of the $MgCl_2$ curve [37]. For the ternary salt, this reaction is confounded with its melting point, at 428.58 °C. Then, for this ternary salt, the dehydrated melting point analyzable in cycle 2 measures 95.97 J/g, so the sum of pure heat of melting and pure MgO precipitation is 172.31 J/g. As the peak of these confounded reactions in cycle 1 reaches 181.7J/g, the identification of MgO formation can be assumed with a relative error of 5%. The recrystallization point when cooling remains decreased from 395.16 °C to 389.62 °C and the melting point to 382.61 °C in cycle 2. Hence, the variation of salt composition due to the formation of MgO does not seem to impact very much on the recrystallization point. The composition of dehydrated salt differs from its initial stage, and the (MgNaK)Cl weight composition becomes 35/29/36 wt% without consideration of Mg volatilization. So, this composition of pure components gives a melting point at 382.62 °C. However, the FactSage ternary phase diagram predicts for this composition a melting point at 450 °C which is not the eutectic. The quantity of $MgCl_2{\cdot}6H_2O$ must be multiplied by 2.53 if we want a relative weight composition of

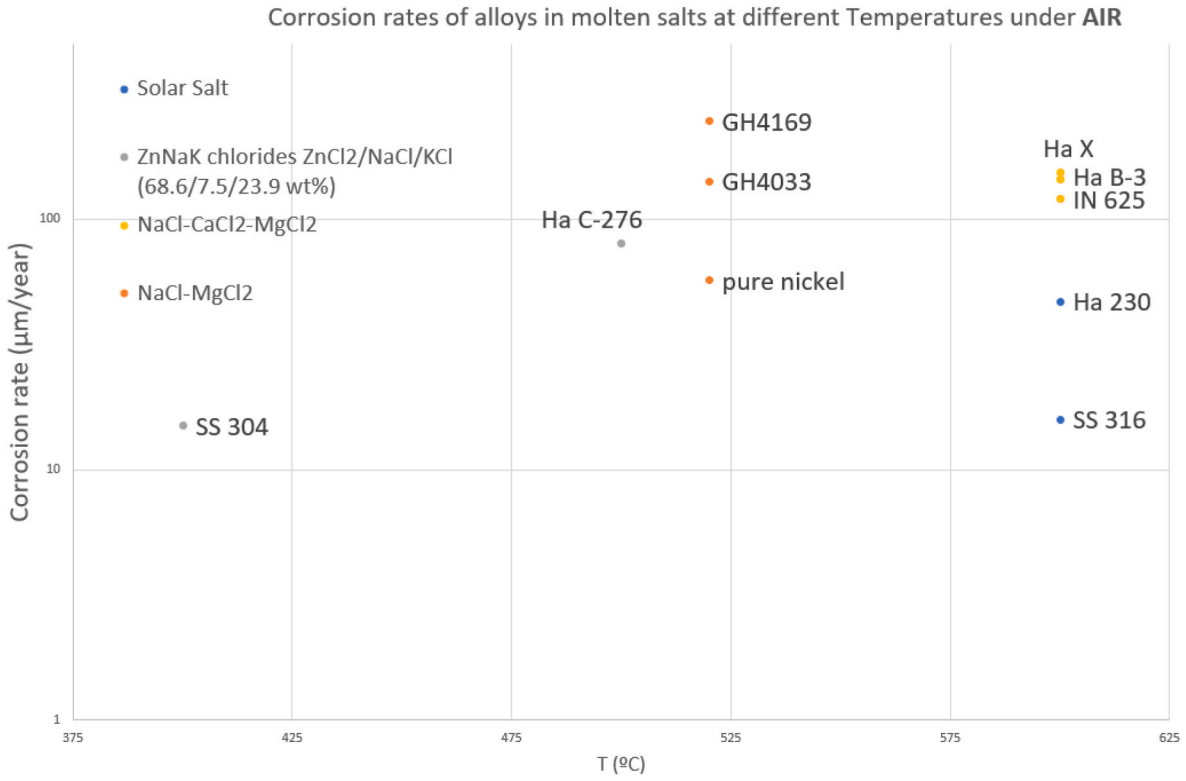

Fig. 15. Corrosion rate of alloys in air under different salts.

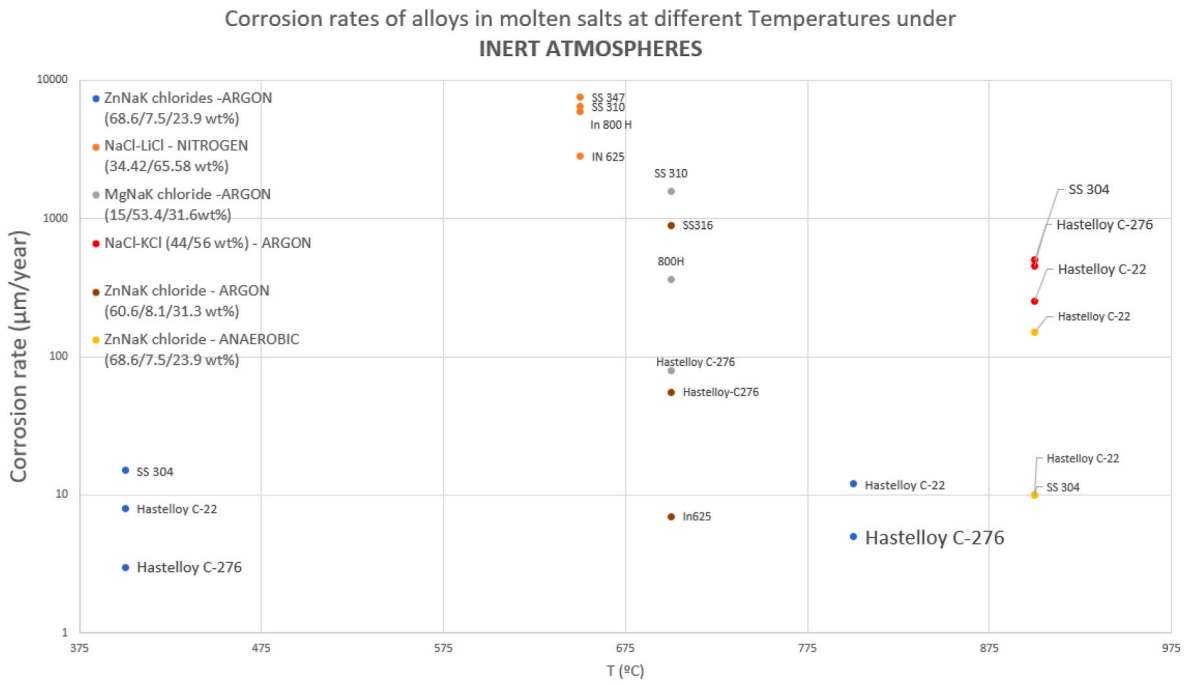

Fig. 16. Corrosion rate of alloys in Argon atmosphere under different salts.

53.41/20.97/25.62 wt%. Therefore, a wise use of ternary phase diagrams whether taking into account the proper dehydration of single salts or not must be considered when choosing a composition. In addition, the volatilization of formed phases tends to give discrepancies from eutectic points.

A numerical simulation with Thermocalc software of the hydrated salt behaviour with temperature is shown on Fig. 14. This software performs calculations from a thermodynamic point of view, providing an idea of the most favoured phases of a material formed in contact with its environment. The dehydration is observable as multiple steps at 100 °C, 200 °C, 260 °C, identifiable as stages I, II and III (reactions (1), (2) and (4)). Interestingly, MgOHCl is already predicted to be formed at 100 °C. Its conversion into MgO is predicted at 460 °C and confirms the identification of DSC measures. The negative values of the MgO amount of the phase may be due to calculation errors. At 480 °C, MgOHCl is totally converted into MgO and the gas phase rises due to HCl formation. Above 490 °C, the salt does not present a variation up to 650 °C, where it is assimilated into an ionic liquid.

Table 4
Parameters of corrosion testings of different alloys.

Alloy	Salt	Method	Testing Temperature (°C)	Time (if specified)	Atmosphere	Corrosion rate (µm/year)	Reference
SS 304	ZnNaK chlorides (68.6/7.5/23.9 wt%)	Isothermal Immersion	400		Argon	15	[7]
Hastelloy C-22			400			8	
Hastelloy C-22			800			12	
Hastelloy C-276			400			3	
Hastelloy C-276			800			5	
SS 347	NaCl–LiCl (34.42/65.58 wt%)		650		Nitrogen	7490	[46]
SS 310			650			6420	
In 800 H			650			5940	
IN 625			650			2800	
SS 310	MgNaK chloride (15/53.4/31.6 wt%)		700	500	Argon	1581	[30]
800H			700			364	
Hastelloy C-276			700			79	
Hastelloy C-276	ZnNaK chloride (68.6/7.5/23.9 wt%)		900	840	Anaerobic	10	[7]
Hastelloy C-22			900			10	
SS 304			900			150	
Hastelloy C-276	NaCl–KCl (44/56 wt%)		900		Argon	450	[7]
Hastelloy C-22			900			250	
SS 304			900			500	
SS316	ZnNaK chloride (60.6/8.1/31.3 wt%)		700	504	Argon	892	[47]
Hastelloy-C276			700	504		55	
In625			700	504		7	

Table 5
Standard reaction potential versus NHE.

Standard reaction	E°(V)
$O_2 + 4H^+ + 4e^- \leftrightarrow 2H_2O$	1,23
$Cu^{2+} + 2e^- \leftrightarrow Cu$	0,34
$2H^+ + 2e^- \leftrightarrow H_2$	0
$Fe^{3+} + 3e^- \leftrightarrow Fe$	−0,04
$Ni^{2+} + 2e^- \leftrightarrow Ni$	−0,257
$Co^{2+} + 2e^- \leftrightarrow Co$	−0,28
$Fe^{2+} + 2e^- \leftrightarrow Fe$	−0,44
$Cr^{3+} + 3e^- \leftrightarrow Cr$	−0,74
$Mn^{2+} + 2e^- \leftrightarrow Mn$	−1,18
$Ti^{2+} + 2e^- \leftrightarrow Ti$	−1,63
$Al^{3+} + 3e^- \leftrightarrow Al$	−1,68

3.2. Corrosion mitigation strategies

Besides the thermal purification explained above, there are chemical and electrochemical strategies that may be also considered for mitigating corrosion.

First, three chemical strategies have been found in literature. To mitigate the formation of magnesium hydroxychloride MgOHCl, it can be thermically reduced with a low additions of Mg [29,35,40]. W. Ding, H. Shi [28] added 1 wt% Mg as a corrosion inhibitor in MgKNa chloride salts and they found a significant reduction in the corrosion rate of Fe–Cr–Ni based alloys, by ~83% for SS 310, ~70% for In 800H and ~94% for Ha C-276, compared with the exposure tests without Mg addition. Moreover, research has been conducted on the dehydration with ammonium chloride [24,37,41–43], and carbochlorination with CO, Cl_2, and/or CCl_4 to remove oxide species, with a content of under 500 micromolal [38,44,45]. The most cost-effective is the first one, Mg additions, even if the concentration parameters have yet to be optimized.

Secondly, the electrochemical method deals with the controlled corrosion of two Mg or W electrodes immersed into the salt, periodically acting as anode and cathode, switching voltage polarization to slow down the cathode passivation [29]. It makes possible to avoid toxic gases such as HCl or Cl_2 but may not stand a high impurity concentration due to fast electrode passivation.

Finally, a thermogravimetric method to evaluate the corrosion rate could be misrepresented because of solid MgO deposition in the chromium depleted zone, as the alloy and the salt should be analysed after the tests.

4. Corrosion behaviour of alloys

High temperature corrosion of tubes and tanks of CSP plants associated with chloride salts is reviewed. As it is relative to salt impurity, different atmospheres on corrosion studies have been tested. To compare with other salts, research conducted on alloys immersed in chloride, solar salts, under air and inert atmosphere at different temperatures have been gathered on Figs. 15 and 16.

4.1. Thermogravimetric testing

When air atmosphere was employed, alloys under NaCaMg chloride salt showed a weaker resistance than under Solar salt [7,39] at 600 °C, with 121.1 μm/year, 144.6 μm/year and 153.2 μm/year for the Inconel 625, Hastelloy B-3, and Hastelloy X, respectively [33]. Thus, those alloys/molten salt pairs cannot be commercialized. Under inert atmosphere, some alloys have found a stronger behaviour against chloride salts. The most remarkable value is the Hastelloy C-276, which showed the best behaviour at 400 °C and 800 °C with 3 and 5 μm/year respectively, under ZnNaK chloride (68.6/7.5/23.9%wt) and argon [7,30]. Indeed, it presented better corrosion resistance under anaerobic conditions than in air (80 μm/year at 500 °C). At 900 °C, Hastelloy C276 and C-22 showed both a corrosion rate of 10 μm/year, and 150 μm/year for SS 304 under ZnNaK chloride (52,9/13,4/33,7%wt). Table 4 gathers the experimental parameters and results of the main systems alloy - chloride mixture studied in literature, including corrosion rates.

4.2. Corrosion mechanisms

The main corrosion process in molten chlorides comes from water contamination and is understandable from standard reduction potentials. Indeed, most reduction potentials of metals in high strength alloys are lower than the ones of proton (0 V versus normal hydrogen electrode (NHE)) and molecular oxygen (1.23 V versus NHE), as seen on Table 5 [48]. The main oxidant is proton from water, as salt dehydration is never totally achieved, even at high temperatures, and to a lesser extent molecular oxygen coming from air leaking into the salt, knowing that O_2 is volatile at high temperatures.

Accordingly the mechanism of corrosion follows this reaction:

$$M(s) + O \rightarrow M^+ + R \text{ where } \left\{ \begin{array}{l} O \text{ is } H^+ \text{ and } R \text{ is molecular hydrogen} \\ or \\ O \text{ is } O^2 \text{ and } R \text{ is } O^{2-} \end{array} \right\} \quad (9)$$

Thus, the production of hydroxychlorides (MgOHCl) and HCl coming from water and air contamination (reaction (3), (5), (7)) are the most corrosive species that need to be controlled.

Also, the reaction (10) tends to form gaseous Cl_2 when exposed to air from 445 °C to 640 °C [41], from $MgCl_2$:

$$MgCl_2 + ½\ O_2 \rightarrow MgO + Cl_2(g) \quad (10)$$

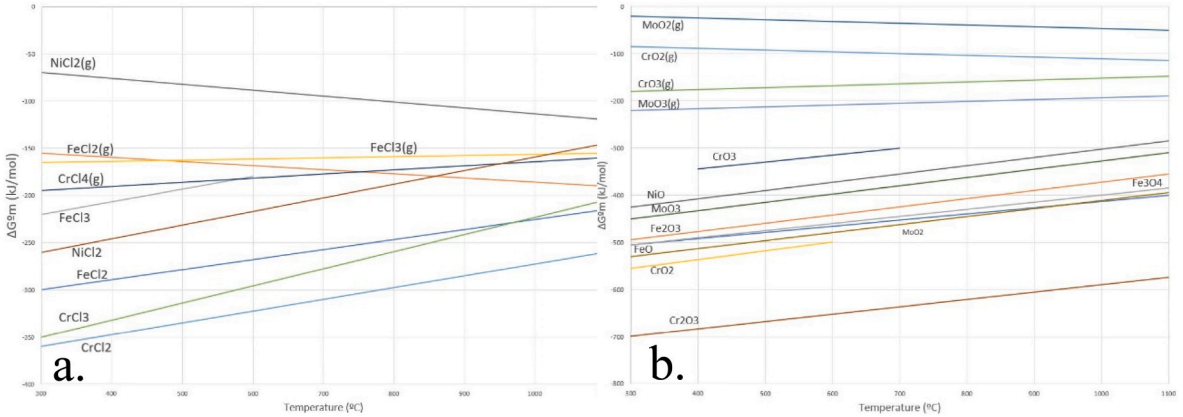

Fig. 17. Gibbs free energy of formation of a. oxides at 1 mol of O2 and b. chloride at 1 mol of Cl2.

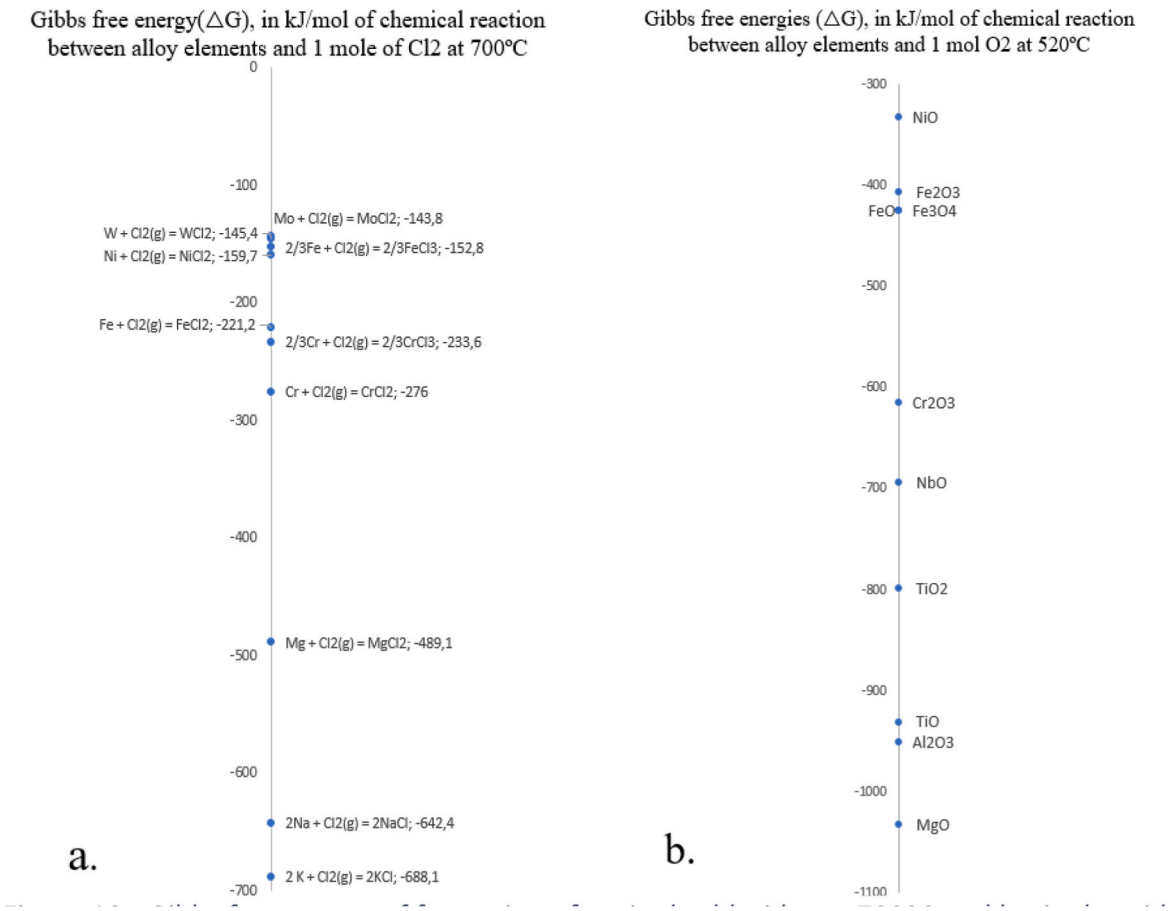

Fig. 18. Gibbs free energy of formation of a. single chlorides at 700 °C and b. single oxides at 520 °C.

Oxygen will form oxide scales, and Cl_2 reactivity can be reduce to Cl^- and thus chlorinate the metal, following reaction (11):

$$M(s) + Cl^- \rightarrow MClx(l,g), \text{ with M the metal element} \quad (11)$$

Thus, the activity of the alloy's elements will be a determining factor and play a well-defined role in the acceleration or mitigation of chloride corrosion against alloys.

The most promising alloys studied are Ni-based alloys [33,34,49–53]. Fig. 17 a. and b. represent the Gibbs free energy of formation of chlorides or oxides according to temperature at 1 mol of O_2 and Cl_2 respectively [33].

Solid iron and chromium oxides and chlorides reactions formation have the highest Gibbs free energy, resulting in their preferential dissolution when immersed into chloride molten salt, whereas the MoO_3 gas phase volatilizes. Then, solid MoO_2 and MoO_3 dissolves first instead of NiO, and this preferential dissolution proved an enhancement in the alloy's corrosion resistance [54]. Chromium has demonstrated an important role in the corrosion [55–60]. The reactions (12) and (13) occur and as the Gibbs free energy of formation is lower by a factor 2 for the formation reaction of chromium oxide than the chromium chloride, with a rather low need of oxygen partial pressure (Fig. 17), the conversion from chloride to oxide chromium occurs, at a small distance from the metal surface [53]. The volatilization of gaseous chlorides and conversions into oxides at the salt/alloy interface is called the "chloridation-oxidation" process [61–63], leading to unprotective and dissolvable multilayers.

$$4Cr_{(s)} + 3O_{2(g)} \rightarrow 4Cr^{3+} + 6O^{2-} \rightarrow 2Cr_2O_{3(s)} \quad (12)$$

$$Cr_{(s)} + Cl_{2(g)} \rightarrow Cr^{2+} + 2Cl^- \rightarrow CrCl_{2(l,g)} \quad (13)$$

The research of Liu and al [33] on Inconel 625 and Hastelloy X revealed that chromium oxide Cr_2O_3 had been destroyed after 5 days of immersion under MgNaCa chloride salt, while a $MgCr_2O_4$ dense layer had shown a protective behaviour. Indeed, the MgO deposition coming from the hydrolyse of impurities reacted in cascade as the following reaction, with their respective Gibbs free energy of reaction [64]:

$$\{MgO(s) \rightarrow Mg2+ + O2^- \text{ (acidic fluxing)}\} \quad (14)$$

$$\{MgO(s) + Cr2O3(s) \rightarrow MgCr2O4(s) \text{ (synergistic dissolution)}\} \quad (15)$$

$$\{Cr2O3(s) + O2- \rightarrow 2CrO2^- \text{ (basic fluxing)}\} \quad (16)$$

$$2CrCl_4(g) + 4MgO(s) \rightarrow MgCr_2O_4(s) + 3MgCl_2(l) + Cl_2(g) \quad (17)$$

$$2MgCr_2O_4(s) + 8MgCl_2(l) + O_2(g) \rightarrow 4CrCl_4(g) + 10MgO(s) \quad (18)$$

Focusing on the microstructure of Ni-based alloys representable as ϒ-Ni grains, intergranular corrosion has been reported to be the main cause of corrosion [64]. Indeed, a sensitization effect occurs resulting in the formation of carbides and inter-metallic phases by the diffusion of carbon towards the grain boundaries, leading to a chromium depletion from the grain to form chromium-containing carbides [60]. Then, there is a Cl_2 gas phase diffusion towards the carbides that leads to their dissolution into the salt, according to reactions [31,46,54,57,58,60,65,66].

$$Cr_7C_3(s) + 7Cl_2(g) + 3O_2 \rightarrow 7CrCl_2 + 3CO_2\ (g) \quad (19)$$

$$Cr_{23}C_6(s) + 23Cl_2(g) + 3O_2 \rightarrow 23CrCl_2 + 6CO(g) \quad (20)$$

$$Cr_{23}C_6(s) + 23Cl_2(g) \rightarrow 23CrCl_2 + 6C(s) \quad (21)$$

Table 6
Chemical composition of potential alloys for corrosion testing under chloride salts.

Alloy	Chemical Composition (wt %)																			
	C	Mn	Fe	S	Si	Ni	Cr	Co	P	Mo	Cu	Al	Ti	Nb	Ta	B	W	V
Already shown good behaviour																		
IN625			5			58	20 to 23	1		8 to 10			0.4	3.15 to 4.15	0.05			
C22	0.002	0.25	3.8	0.004	0.03	57.36	21.2	0.93	0.007	13.3							2.9	
C276	0.02	0.1	4 to 7	0.03	0.08	60.39	14.5 to 16.5	2.5	0.03	15 to 17							3 to 4.5	0.35
Potential alloys against chloride molten salts																		
Alloy 740	0.03	0.3	0.2		0.15	50	24.6	20.1		0.5		1.4	1.45	1.47				
IN617	0.15	0.5	3.0	0.015	0.5	44.2–56.0	20.0–24.0	10.0–15.0	0.015	8.0–10.0	0.5	0.8–1.5	0.6			0.006		
Haynes 242	0.003	0.33	1.02		<0.05	65.79	8.01	<0.05		24.9		0.15						

As a result, a higher content in chromium allows a larger chemical potential gradient and activity and thus the formation of Cr-carbides [67], so the mitigation of these phases must be taken into account. In parallel, Mo- and W- rich carbides have also been detected at grain boundaries [34,68,69]. While their Gibbs free energy of chlorides formation is similar at 700 °C Fig. 18.a., their influence varies. Numerical simulations have been performed on alloys 230, and tungsten chemical potential increases with chromium, so their relation predicts the same behaviour for W as Cr-rich carbides [70]. Indeed, the Cr depletion by Cr-carbides dissolution enhances the carbon activity that drives the W-carbide dissolution. Plus, W-carbides have not shown any influence on the chromium depletion along grain boundaries, while Mo-carbides are stable and do not dissolves into the salt, which can prevent Cr diffusion. Moreover, Ni–Mo–Cr showed a better behaviour than Ni–W–Cr [34]. Indeed, the solid-state diffusion of Mo permits its transfer to fill the vacancies created by Cr depletion, and creates a barrier preventing Cr outward diffusion, whereas W has not shown this behaviour, with a slower diffusion, due to its larger size.

Ti, Ta and Nb refractory metals in Ni-based alloys have been found to form MC type stable carbides instead of chromium, which can prevent its depletion [71], and to precipitate δ-Ni_3Nb at grain boundaries and Ti strong carbides and carbonitrides species from the ϒ substrate that are not dissolved during anodic oxidation [50,61,72]. Ti and Al were found to create a compact and steady oxide layer on GH4033 under NaMg chloride salt at 520 °C, as their Gibbs free energy of formation is similar and close to that of Mg (Fig. 18.b.). However, for GH4169, the rich Nb-δ boundary phase was corroded preferentially, acting as the mass transfer channel of molten salt [50].

It is well-known that the formation of σ phases induces a lower resistance on pitting corrosion and undesirable mechanical properties [73–76]. Si was found to intensify the formation of Cr–Mo σ-phases at grain boundaries when added from 0.4 wt% to 1 wt% in a Cr–Ni–Mo super austenitic stainless steel, significantly increasing the activity of Mo, and thus the surrounding Cr and Mo depletion [74].

Research has been conducted on the optimization of alloying refractory elements and cobalt in chloride salts [77]. It resulted in a 10–20-time diminution of the chromium concentration in the salt with 12% refractory metals forming stable spinels or 18% cobalt acting as a barrier, preventing chromium outward diffusion and anionic oxide inward diffusion. A Cr(II) and Ta(V) stable compound exhibited passivation, whereas Mn was present in anodic dissolution [72].

Aluminium in chloride salts has shown different behaviors depending on its testing atmosphere. Indeed, pre-oxidized Al–FAs In702 in oxygen containing atmosphere showed a 13 μm growth after 185 h of cycled immersion from 550 °C to 700 °C, while alumina layers were unstable and spalled off when testing under Argon atmosphere [78]. Al_2O_3, SiO_2 and TiO_2 are stable oxides under oxidizing-chloridizing atmosphere if sufficient oxygen partial pressure is present ($p(O_2) \geq 0{,}2$ bar) [63].

5. Thermodynamic simulations of promising alloy – molten chloride systems

In625, C22 and C276 are the alloys that have already demonstrated interesting behaviours. The choice of potential materials is summarised in Table 6. Alloy 740, Haynes 242 and In617 are the promising alloys relying on the different studies on alloying elements presented above. Indeed, research will be conducted on Ni-based alloy with low content of iron, silicon, manganese, and carbon. Different concentrations of chromium, cobalt and molybdenum are chosen to study their counterbalance effect on the dissolution of chromium, with no tungsten. Plus, these Ti–Nb's, Ti's containing and not containing rare-earth metals alloys will make it possible to compare the influence of their formed phases. To better estimate the phases formed, a Thermocalc simulation is performed, with the interactions of Alloy 740, Haynes 242 and In617 against MgNaK (53.41/20.97/25.62 wt%) chloride and ZnNaK (68.67/

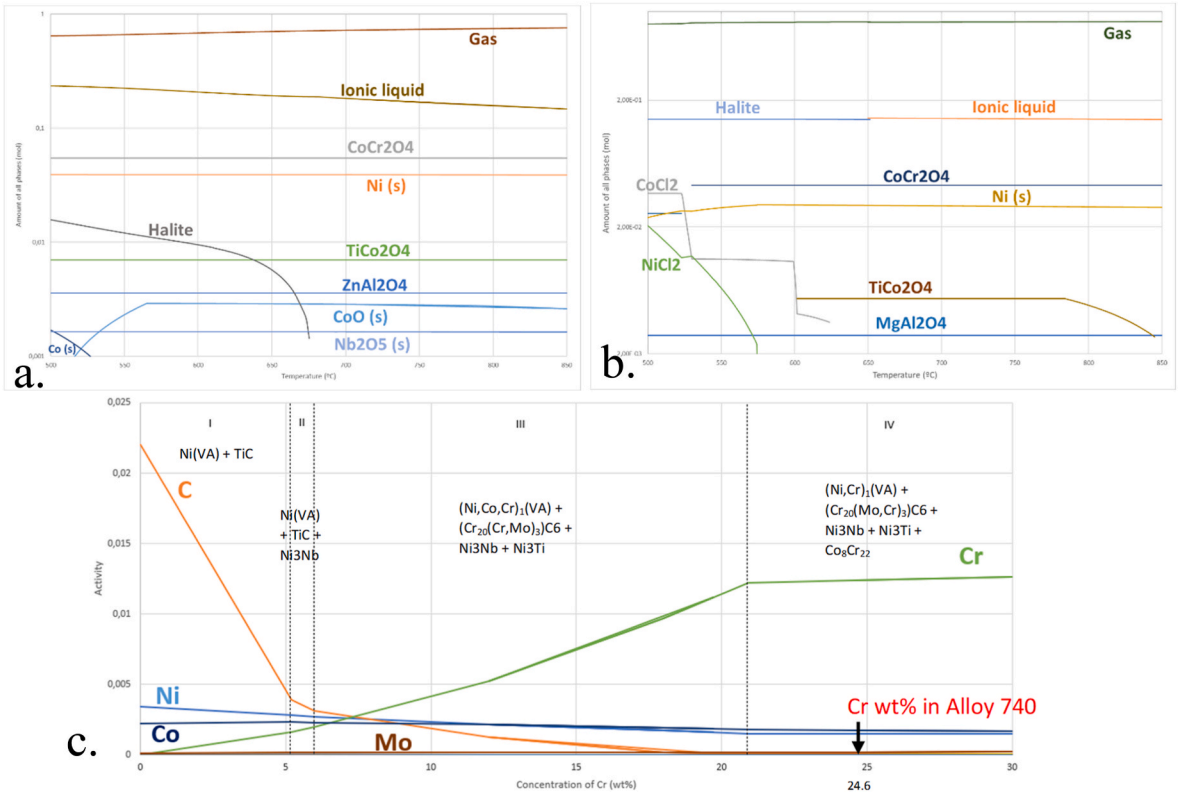

Fig. 19. Calculated amount of phases formed at the interface a. (ZnNaK)Cl-Alloy 740, b. (MgNaK)Cl-Alloy 740 c. Calculated activities of Alloy 740 elements in accordance with the chromium concentration.

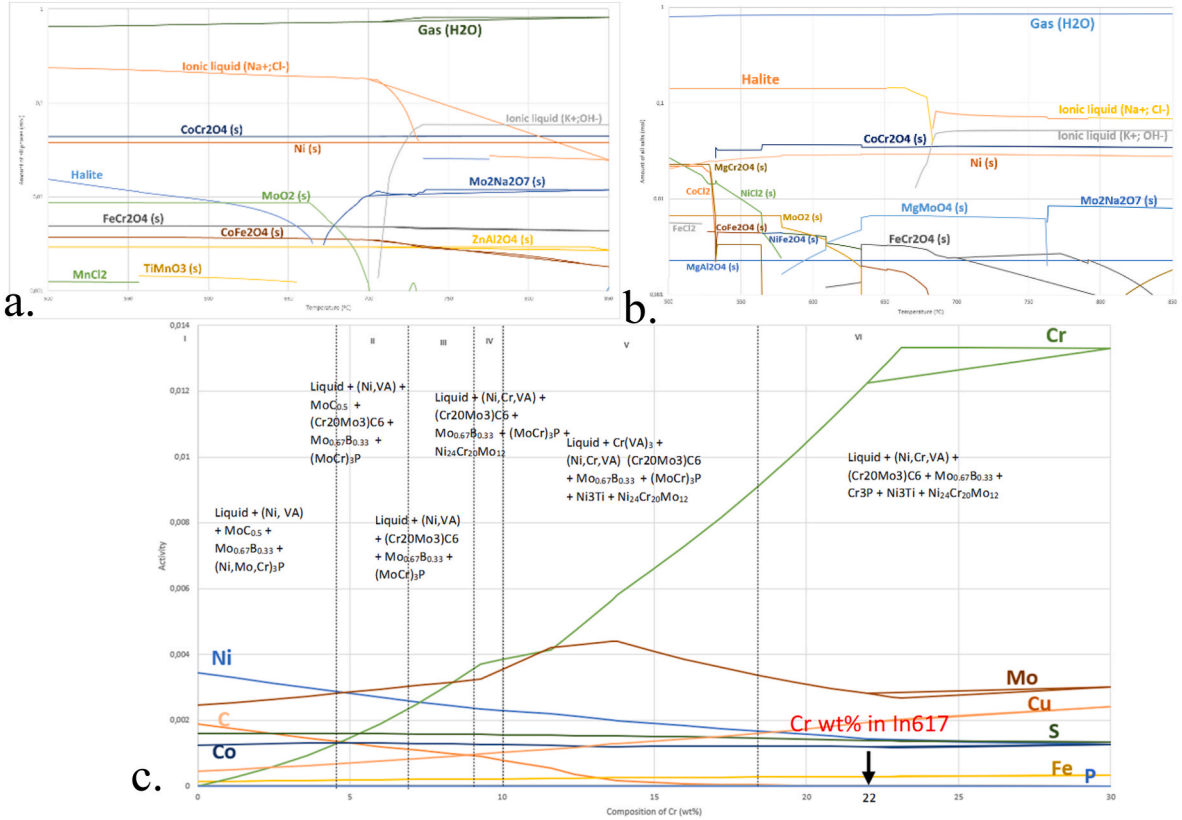

Fig. 20. Calculated amount of phases formed at the interface a. (ZnNaK)Cl-IN617, b. (MgNaK)Cl-IN617 c. Calculated activities of IN617 elements in accordance with the chromium concentration.

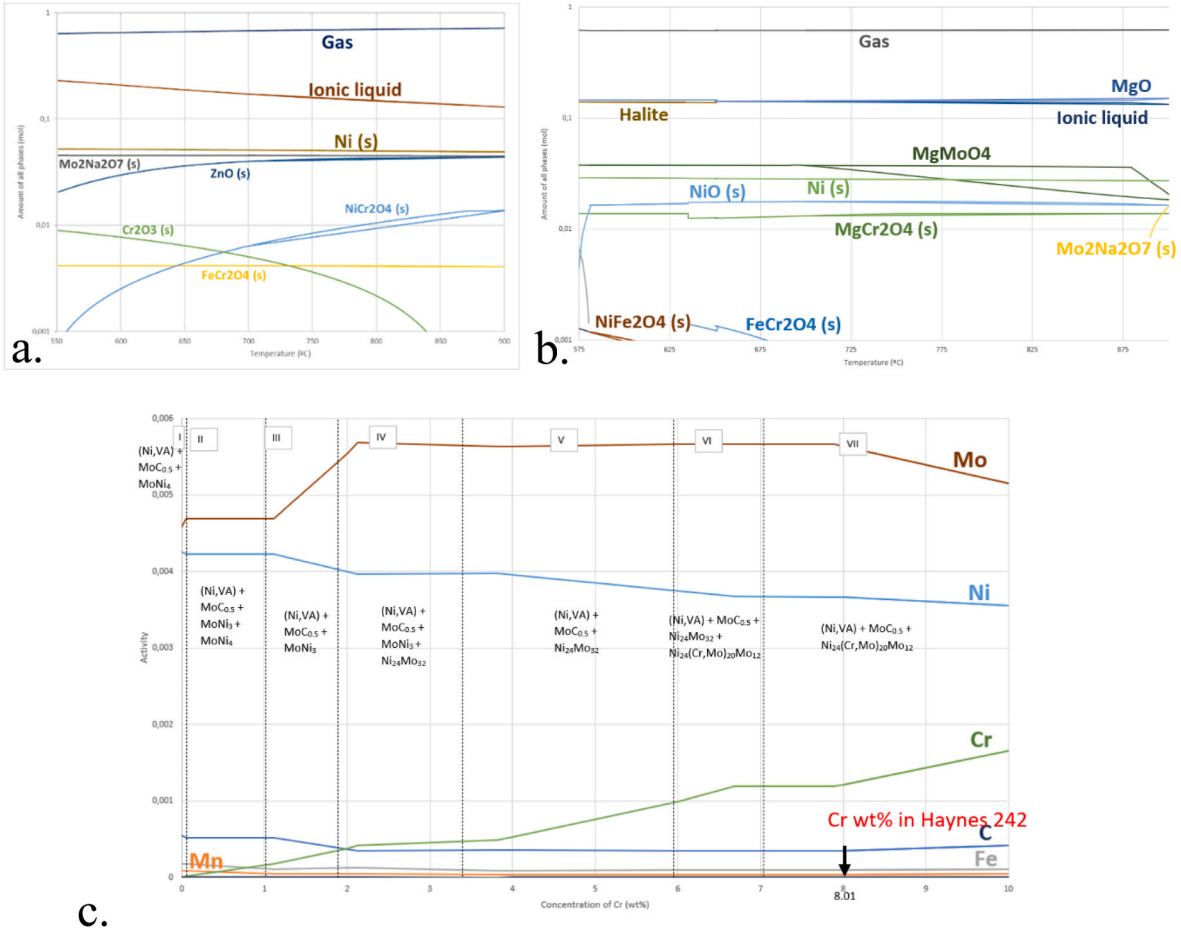

Fig. 21. Calculated amount of phases formed at the interface a. (ZnNaK)Cl–H242, b. (MgNaK)Cl–H242 c. Calculated activities of H242 elements in accordance with the chromium concentration.

7.22/24.10 wt%) chloride, which also represent a great HTF potential thanks to their operating range.

5.1. Numerical simulations

Thermocalc software was used to plot:

1. Activities of elements in those three selected alloys according to the chromium concentration at 650 °C, to predict the behaviour of the materials and their potential phases which may be formed inside the bulk.
2. Reactions between hydrated (MgNaK)Cl and (ZnNaK)Cl salts with these alloys at the interface, in the temperature range [500°C-875 °C].

Indeed, the influence of the amount of each alloying elements on their activities is clearly observable. Chromium depletion is induced by its activity and the more it is present in the alloy, the more it rises. Firstly, Alloy 740 (Fig. 19) presents a major activity of chromium (0.012) followed by similar activities of cobalt and nickel (0.002) that are independent of chromium concentration and constant. Therefore, they would tend to form phases such as the Co–Cr σ-phase, ϒ'-Ni3Ti, δ-Ni3Nb precipitation, Cr–Mo carbides, and Ni–Cr phase. Indeed, chromium depletion could induce the rise of carbon activity leading to carbides dissolution but giving way to the formation of potentially protective Ni and Ni–Co phases. Calculations at the interface with the salt confirm the presence of $CoCr_2O_4$ spinel, and Ni phase in majority; titanium would also participate with the formation of $TiCo_2O_4$ spinel. Aluminium tends to react with the II + cation elements present in the salt to form $ZnAl_2O_4$ and $MgAl_2O_4$, respectively. Finally, niobium also plays a role with the formation of an oxide Nb_2O_5 in (ZnNaK)Cl but in a minor quantity.

Secondly, In617 (Fig. 20) also presents a larger activity of chromium (0.013) but a stronger one of molybdenum (0.003), stemming from its composition (8–10 wt%), followed by copper (0.002) and cobalt-nickel-sulphur (~0.0015). The related phases are P-phase Ni–Cr–Mo, ϒ'-Ni3Ti, Cr3P, tetragonal Mo–B, Cr–Mo carbides, and Ni–Cr phase. Moreover, cobalt activity remains stable while copper decreases and nickel and carbon rise with chromium depletion. Calculation at the interface also predicts a majority of $CoCr_2O_4$ spinel and Ni phases. Moreover, there is a tendency of formation of Mo-phases, such as MoO_2 converting into $Mo_2Na_2O_7$ at 700-750 °C, or $MgMoO_4$. Iron spinels are present as $FeCr_2O_4$, $CoFe_2O4$ or $NiFe_2O_4$ and aluminium also predicts the formation of spinels with Zn^{2+} and Mg^{2+}. Plus, $TiMnO_3$ is calculated with Zn-Salt in a small quantity.

Finally, Haynes 242 (Fig. 21) has an activity driven by molybdenum (0.0057), originating from its high concentration (24.9 wt%), followed by nickel (0.0037), chromium (0.0012) and carbon (0.0003). The related phases are P-phase Ni–Cr–Mo, hexagonal close-packed (hcp) Mo–C and Ni-phase. The activity of nickel seems related to that of chromium, as they present a symmetry, while Mo activity decreases. Indeed, chromium depletion leads to a proportional rise of nickel activity leading to the cascade formation of δ-(Mo32Ni24), γ-(MoNi3) and β-(MoNi4), while the P-phase disappears, and hcp-Mo-C remains. Calculations at the interface predict different behaviors with salts. For (ZnNaK)Cl, Ni, $Mo_2Na_2O_7$ and ZnO phases are in majority. Then,

NiCr2O4 spinel is formed with the diminution of Cr_2O_3 and thus with its reaction with NiO. Plus, $FeCr_2O_4$ is present in minority. For (MgNaK)Cl, MgO, $MgMoO_4$, and Ni phases are in majority, followed by NiO and $MgCr_2O_4$. Moreover, $Mo_2Na_2O_7$ is formed above 875 °C and $NiFe_2O_4$ and $FeCr_2O_4$ spinel are not stable above 600 °C and 675 °C, respectively.

6. Conclusions

Chloride salts are high potentials for HTF in CSP plants, with MgNaK and ZnNaK chlorides for the most promising of them, due to their low melting point and wide operation ranges. In order to select a cost-effective and performant one, with nano-addition, what is needed are preliminary characterization studies, such as their specific heat, thermal conductivity and viscosity. Additions of Al_2O_3, SiO_2, expanded graphite, and MWCNTs nanoparticles need to be explored.

Furthermore, hygroscopic single salts as $MgCl_2{\cdot}6H_2O$ and $ZnCl_2{\cdot}4H_2O$ need to be purified to avoid the formation of corrosive species. The multistep dehydration process has been confirmed with DSC measurements and it could be a method to determine the heating steps of each water-containing salt. In parallel, numerical simulations on Thermocalc software confirmed this process. Moreover, some ternary phase diagrams do not have specifications on their consideration on hydrates containing salts, giving irrelevant graphical pointing and DSC/TGA measurements are necessary to evaluate it. Plus, discrepancies on eutectic points must be minimized with the formation of hydroxy chlorides. Indeed, the choice of a potential alloy in contact with molten chlorides must be made with the strain of water or oxygen presence for the CSP plant scale. Previous studies have already demonstrated some great durability against molten chlorides under inert atmospheres with C276, C22 and In625 and research conducted on element behaviour has made it possible to choose potential alloys, such as Alloy 740, In617 and H242. Thermocalc simulations of the interactions between these alloys and the chosen salts presented the most favoured phases formed at a high temperature. It remains to be seen if those phases occur in a real test and are protective over time.

Data availability

The data that support the findings of this study are available from the corresponding author, Mickaël Lambrecht, upon reasonable request.

Declaration of competing interest

The authors declare the following financial interests/personal relationships which may be considered as potential competing interests: Ángel G. Fernández (GREiA Research Group INSPIRES Research Centre, Lleida University and Energy Development Center, **University of Antofagasta**)Luisa F. Cabeza (GREiA Research Group INSPIRES Research Centre, **University of Lleida**) Héctor R. Galleguillos (Chemical Engineering and Mining Processes Department, **University of Antofagasta**)Edward Fuentealba (Chemical Engineering and Mining Processes Department, **University of Antofagasta**)Cristina Prieto (**Abengoa** and **University of Sevilla**)F. Javier Ruiz-Cabañas (**Abengoa** and **University of Sevilla**).

Acknowledgments

This work received funding from the European Union's Horizon 2020 research and an innovation program under grant agreement No.686008, project RAISELIFE.

This work received funding from the Agencia Estatal de Investigación in the frame of the "Proyectos I + D + i 2020" programme and under project reference number PID2020-115866RB-C22 (PID2020-115866RB-C22/AEI/10.13039/501100011033).

References

[1] M.D. Carlson, B.M. Middleton, C.K. Ho, Techno-economic comparison of solar-driven SCO2 Brayton cycles using component cost models baselined with vendor data and estimates, in: ASME 2017 11th International Conference on Energy Sustainability, June 26-30, 2017, p. 7.
[2] G. Mohan, M.B. Venkataraman, J. Coventry, Sensible energy storage options for concentrating solar power plants operating above 600 °C, Renew. Sustain. Energy Rev. 107 (2019) 319–337.
[3] X. Xu, et al., Basic properties of eutectic chloride salts NaCl-KCl-ZnCl2 and NaCl-KCl-MgCl2 as HTFs and thermal storage media measured using simultaneous DSC-TGA, Sol. Energy 162 (2018) 431–441.
[4] S. Kuravi, et al., Thermal energy storage technologies and systems for concentrating solar power plants, Prog. Energy Combust. Sci. 39 (4) (2013) 285–319.
[5] Y. Zhang, P. Li, Minimum system entropy production as the FOM of high temperature heat transfer fluids for CSP systems, Sol. Energy 152 (2017) 80–90.
[6] D. Lide, Physical constants of inorganic compounds, CRC Handbook of Chemistry and Physics (2006) 60.
[7] K. Vignarooban, et al., Vapor pressure and corrosivity of ternary metal-chloride molten-salt based heat transfer fluids for use in concentrating solar power systems, Appl. Energy 159 (2015) 206–213.
[8] M.W. Chase, Jr. NIST-JANAF Thermochemical Tables. 4th Ed. J. Phys. Chem. Ref. Data, Monograph 9, National Institute of Standards and Technology (NIST), 1998. Gaithersburg, MD.
[9] C. Li, et al., Survey of properties of key single and mixture halide salts for potential application as high temperature heat transfer fluids for concentrated solar thermal power Systems+, AIMS Energy (2014) 25.
[10] Q. Yan, et al., Study on preparation and thermal properties of mixed chloride salts, Thermochim. Acta 690 (2020) 178689.
[11] C. Robelin, P. Chartrand, Thermodynamic evaluation and optimization of the (NaCl+KCl+MgCl2+CaCl2+ZnCl2) system, J. Chem. Therm. 43 (3) (2011) 377–391.
[12] A. Ibrahim, et al., Molten salts in the light of corrosion mitigation strategies and embedded with nanoparticles to enhance the thermophysical properties for CSP plants, Sol. Energy Mater. Sol. Cell. 219 (2021) 110768.
[13] H.A. Aljaerani, et al., Thermo-physical properties and corrosivity improvement of molten salts by use of nanoparticles for concentrated solar power applications: a critical review, J. Mol. Liq. 314 (2020) 113807.
[14] D. Han, et al., Thermal properties characterization of chloride salts/nanoparticles composite phase change material for high-temperature thermal energy storage, Appl. Energy 264 (2020) 114674.
[15] H. Tian, et al., Enhanced specific heat of chloride salt with Mg particles for high-temperature thermal energy storage, Energy Proc. 105 (2017) 4402–4407.
[16] Y. Wu, et al., Solar salt doped by MWCNTs as a promising high thermal conductivity material for CSP, RSC Adv. (2018) 10.
[17] H. Tian, et al., Thermal conductivities and characteristics of ternary eutectic chloride/expanded graphite thermal energy storage composites, Appl. Energy 148 (2015) 87–92.
[18] Z. Zhang, et al., Enhanced thermal properties of Li2CO3Na2CO3K2CO3 nanofluids with nanoalumina for heat transfer in high-temperature CSP systems, Therm Anal Calorim (2017) 10.
[19] Y. Ueki, et al., Molten salt thermal conductivity enhancement by mixing nanoparticles, Fusion Eng. Des. 136 (2018) 1295–1299.
[20] Y. Ueki, et al., Thermal conductivity of molten salt-based nanofluid, AIP Adv. (2017) 8.
[21] M. Lasfargues, et al., Rheological analysis of binary eutectic mixture of sodium and potassium nitrate and the effect of low concentration CuO nanoparticle addition to its viscosity, Mater. Corros. (2015) 11.
[22] S. Jung, Numerical and experimental investigation of inorganic nanomaterials for thermal energy storage (TES) and concentrated solar power (CSP) applications, 2012, p. 235.
[23] N. Navarrete, et al., Influence of the production method on the thermophysical properties of high temperature molten salt-based nanofluids, J. Mol. Liq. 302 (2020) 112570.
[24] G.J. Kipouros, D.R. Sadoway, A thermochemical analysis of the production of anhydrous MgCl2, J. Light Met. 1 (2) (2001) 111–117. Pubmed Partial Author articletitle stitle stitle Volume Issue Page.
[25] W. Ding, T. Bauer, Progress in research and development of molten chloride salt technology for next generation concentrated solar power plants, Engineering (2021).
[26] J.C. Vidal, N. Klammer, in: Molten Chloride Technology Pathway to Meet the U.S. DOE Sunshot Initiative with Gen3 CSP. AIP Conference Proceedings, 2019, p. 10.
[27] W. Ding, et al., Molten chloride salts for next generation CSP plants: electrolytical salt purification for reducing corrosive impurity level, Sol. Energy Mater. Sol. Cell. 199 (2019) 8–15.
[28] W. Ding, et al., Molten chloride salts for next generation concentrated solar power plants: mitigation strategies against corrosion of structural materials, Sol. Energy Mater. Sol. Cell. 193 (2019) 298–313.
[29] W. Ding, et al., Molten chloride salts for high-temperature thermal energy storage: continuous electrolytic salt purification with two Mg-electrodes and alternating voltage for corrosion control, Sol. Energy Mater. Sol. Cell. 223 (2021) 110979.
[30] W. Ding, et al., Hot corrosion behavior of commercial alloys in thermal energy storage material of molten MgCl2/KCl/NaCl under inert atmosphere, Sol. Energy Mater. Sol. Cell. 184 (2018) 22–30.

[31] H. Sun, P. Zhang, J. Wang, Effects of alloying elements on the corrosion behavior of Ni-based alloys in molten NaCl-KCl-MgCl2 salt at different temperatures, Corrosion Sci. 143 (2018) 187–199.
[32] W. Ding, et al., Cyclic voltammetry for monitoring corrosive impurities in molten chlorides for thermal energy storage, Energy Proc. 135 (2017) 82–91.
[33] B. Liu, et al., Corrosion behavior of Ni-based alloys in molten NaCl-CaCl2-MgCl2 eutectic salt for concentrating solar power, Sol. Energy Mater. Sol. Cell. 170 (2017) 77–86.
[34] H. Sun, et al., Corrosion behavior of 316SS and Ni-based alloys in a ternary NaCl-KCl-MgCl2 molten salt, Sol. Energy 171 (2018) 320–329.
[35] H. Sun, et al., Assessment of effects of Mg treatment on corrosivity of molten NaCl-KCl-MgCl2 salt with Raman and Infrared spectra, Corrosion Sci. 164 (2020) 108350.
[36] Smith, Veazey, Dehydration of Magnesium Chloride/patent, 1931, p. 12.
[37] Z. Zhang, et al., The dehydration of MgCl2·6H2O by inhibition of hydrolysis and conversion of hydrolysate, J. Anal. Appl. Pyrol. 138 (2019) 114–119.
[38] I. Wen Sun, K.D. Sienerth, G. Mamantov, The use of phosgene for the removal of oxide impurities from a sodium chloroaluminate melt saturated with sodium chloride, J. Electrochem. Soc. (1991) 32.
[39] K. Vignarooban, et al., Heat transfer fluids for concentrating solar power systems – a review, Appl. Energy 146 (2015) 383–396.
[40] Y. Zhao, J. Vidal, Potential scalability of a cost-effective purification method for MgCl2-Containing salts for next-generation concentrating solar power technologies, Sol. Energy Mater. Sol. Cell. 215 (2020) 110663.
[41] H.C. Eom, H. Park, H.S. Yoon, Preparation of anhydrous magnesium chloride from ammonium magnesium chloride hexahydrate, Adv. Powder Technol. 21 (2) (2010) 125–130.
[42] N.B. Zhou, et al., Preparation and characteristic research of anhydrous magnesium chloride with dehydrated ammonium carnallite, J. Cent. South Univ. Technol (2006) 6.
[43] Z. Zhang, et al., Preparation of anhydrous magnesium chloride from ammonium carnallite, Mater. Manuf. Process. (2013) 6.
[44] R.T. Mayes, et al., Purification of chloride salts for concentrated solar power applications, ORNL (2018) 21.
[45] J.M. Kurley, et al., Enabling chloride salts for thermal energy storage: implications of salt purity, RSC, RSC Adv. (2019) 7.
[46] J.C. Gomez-Vidal, R. Tirawat, Corrosion of alloys in a chloride molten salt (NaCl-LiCl) for solar thermal technologies, Sol. Energy Mater. Sol. Cell. 157 (2016) 234–244.
[47] X. Zhuang, W. Liu, X. Xu, Hot corrosion of different alloys in chloride and carbonate molten-salt mixtures under argon atmosphere, Sol. Energy 189 (2019) 254–267.
[48] C.M.A. Brett, Standard electrode potentials and application to characterization of corrosion phenomena, Encyclopedia of Interfacial Chemistry (2018).
[49] Q. Liu, et al., Ni-Mo-Cr alloy corrosion in molten NaCl-KCl-MgCl2 salt and vapour, Corrosion Sci. 180 (2021) 109183.
[50] J.W. Wang, et al., Corrosion behavior of nickel-based superalloys in thermal storage medium of molten eutectic NaCl-MgCl2 in atmosphere, Sol. Energy Mater. Sol. Cell. 164 (2017) 146–155.
[51] B. D'Souza, et al., Corrosion behavior of boronized nickel-based alloys in the molten chloride Salt, Corrosion Sci. 182 (2021) 109285.
[52] D. Deb, S.R. Iyer, V.M. Radhakrishnan, A comparative study of oxidation and hot corrosion of a cast nickel base superalloy in different corrosive environments, Mater. Lett. 29 (1) (1996) 19–23.
[53] A. Zahs, M. Spiegel, H.J. Grabke, Chloridation and oxidation of iron, chromium, nickel and their alloys in chloridizing and oxidizing atmospheres at 400–700°C, Corrosion Sci. 42 (6) (2000) 1093–1122.
[54] S. Liu, et al., A comparative study on the high temperature corrosion of TP347H stainless steel, C22 alloy and laser-cladding C22 coating in molten chloride salts, Corrosion Sci. 83 (2014) 396–408.
[55] Y.S. Li, M. Spiegel, S. Shimada, Corrosion behaviour of various model alloys with NaCl–KCl coating, Mater. Chem. Phys. 93 (1) (2005) 217–223.
[56] T. Ishitsuka, K. Nose, Stability of protective oxide films in waste incineration environment—solubility measurement of oxides in molten chlorides, Corrosion Sci. 44 (2) (2002) 247–263.
[57] A. Chyrkin, et al., Modeling carbide dissolution in alloy 602 CA during high temperature oxidation, Corrosion Sci. 96 (2015) 32–41.
[58] S.K. Gill, et al., Investigating corrosion behavior of Ni and Ni-20Cr in molten ZnCl2, Corrosion Sci. 179 (2021) 109105.
[59] B. D'Souza, et al., Impurity driven corrosion behavior of HAYNES® 230® alloy in molten chloride salt, Corrosion Sci. (2021) 109483.
[60] A.V. Abramov, et al., Corrosion of austenitic stainless steels in chloride melts, Molten Salts Chemistry and Technology (2014) 22. Pubmed Partial Author articletitle stitle stitle Volume Page.
[61] B. Grégoire, et al., Corrosion mechanisms of ferritic-martensitic P91 steel and Inconel 600 nickel-based alloy in molten chlorides. Part I: NaCl–KCl binary system, Sol. Energy Mater. Sol. Cell. 215 (2020) 110659.
[62] H.J. Grabke, E. Reese, M. Spiegel, The effects of chlorides, hydrogen chloride, and sulfur dioxide in the oxidation of steels below deposits, Corrosion Sci. 37 (7) (1995) 1023–1043.
[63] R. Bender, M. Schütze, The role of alloying elements in commercial alloys for corrosion resistance in oxidizing-chloridizing atmospheres Part I: literature evaluation and thermodynamic calculations on phase stabilities, Mater. Corros. (2003) 20. Pubmed Partial Author articletitle stitle stitle Volume Page.
[64] B. Grégoire, et al., Corrosion mechanisms of ferritic-martensitic P91 steel and Inconel 600 nickel-based alloy in molten chlorides. Part II: NaCl-KCl-MgCl2 ternary system, Sol. Energy Mater. Sol. Cell. 216 (2020) 110675.
[65] M. Hofmeister, et al., Corrosion behaviour of stainless steels and a single crystal superalloy in a ternary LiCl–KCl–CsCl molten salt, Corrosion Sci. 90 (2015) 46–53.
[66] A.V. Abramova, et al., Corrosion of corrosion-resistant and high-temperature nickel-based alloys in chloroaluminate melts, ECS Transactions (2014) 10.
[67] R. Pillai, S.S. Raiman, B.A. Pint, First steps toward predicting corrosion behavior of structural materials in molten salts, J. Nucl. Mater. 546 (2021) 152755.
[68] Z. Qiu, et al., Effects of post heat treatment on the microstructure and mechanical properties of wire arc additively manufactured Hastelloy C276 alloy, Mater. Char. (2021) 111158.
[69] J. He, et al., On the compositional and structural redistribution during partial recrystallisation: a case of σ-phase precipitation in a Mo-doped NiCoCr medium-entropy alloy, Scripta Mater. 194 (2021) 113662.
[70] A. Jalowicka, et al., Effect of specimen thickness on microstructural changes during oxidation of the NiCrW alloy 230 at 950–1050C, The Minerals, Metals & Materials Society (2015) 16.
[71] G. Prashar, H. Vasudev, Hot corrosion behavior of super alloys, Mater. Today Proc. 26 (2020) 1131–1135.
[72] A.V. Abramov, et al., Spectroelectrochemical study of stainless steel corrosion in NaCl-KCl melt, The Electrochemical Society (2010).
[73] D.D.S. Silva, et al., Microstructural influence of sigma phase on pitting corrosion behavior of duplex stainless steel/NaCl electrolyte couple, Mater. Chem. Phys. 259 (2021) 124056.
[74] C. Lee, et al., Influence of Si on sigma phase precipitation and pitting corrosion in superaustenitic stainless steel weld metal, Mater. Chem. Phys. 207 (2018) 91–97.
[75] D.H. Chung, X.D. Liu, Y. Yang, Fracture of sigma phase containing Co–Cr–Ni–Mo medium entropy alloys, J. Alloys Compd. 846 (2020) 156189.
[76] L.H. Guilherme, et al., Effect of MAG welding transfer mode on sigma phase precipitation and corrosion performance of 316L stainless steel multi-pass welds, J. Mater. Res. Technol. 9 (5) (2020) 10537–10549.
[77] A.M. Kruizenga, Corrosion mechanisms in chloride and carbonate salts, SANDIA REPORT (2012) 34.
[78] J.C. Gomez-Vidal, et al., Corrosion resistance of alumina forming alloys against molten chlorides for energy production, II (Int. Immunol.): Electrochemical impedance spectroscopy under thermal cycling conditions. Solar Energy Materials and Solar Cells 166 (2017) 234–245.